UNIVERSITY OF CALIFORNIA SAN DIEGO

A Universal Understanding of Thermal Quenching in Eu^{2+} and Ce^{3+}-Doped Phosphors

A thesis submitted in partial satisfaction of the requirements for the degree Master of Science

in

Materials Science and Engineering

by

Mahdi Amachraa

Committee in charge:

Professor Shyue Ping Ong, Chair
Professor Olivia Graeve
Professor Joanna Mckittrick

2019

The Thesis of Mahdi Amachraa is approved, and it is acceptable in quality and form for publication on microfilm and electronically:

_____

_____

_____

Chair

University of California San Diego

2019

DEDICATION

This thesis is dedicated to my parents, Zhenbin Wang and Casey Lauren Weaver.

EPIGRAPH

Divide each difficulty into as many parts as is feasible and necessary to resolve it.

- René Descartes

TABLE OF CONTENTS

LIST OF FIGURES

LIST OF TABLES

ACKNOWLEDGMENTS

First of all, I would like to express my sincere gratitude to my advisor, Dr. Shyue Ping Ong, for first giving me the opportunity to study and investigate fields that personally matter to me. Working under Dr. Shyue Ping Ong is empowering and inspiring me to become the leader I would like to become in my future career. I also sincerely thank Dr. Graeve and Dr. Mckittrick for their useful suggestions during our numerous research meetings. A very special gratitude goes to Dr. Wang who has accepted the ultimate challenge to mentor and thoroughly guide me during my work.

Secondly, I would like to thank my collaborators, Dr. Chen, and Miss Hanmei Tang for their critical thinking. I also would like to thank all the technical staff at the San Diego Super Computer and NERSC.

Finally, I would like to thank my parents and friends for their support and patience.

The full content of the thesis is currently being prepared for submission for publication of the material. Zhenbin Wang, Hanmei Tang, Chi Chen, and Shyue Ping Ong. The thesis author was the primary investigator and author of this material.

ABSTRACT OF THE THESIS

A Universal Understanding of Thermal Quenching in Eu^{2+} and Ce^{3+}-Doped Phosphors

by

Mahdi Amachraa

Master of Science in Materials Science and Engineering

University of California San Diego, 2019

Professor Shyue Ping Ong, Chair

Phosphor-converted white light-emitting diodes (pc-WLEDs) have been widely adopted for next-generation solid-state lighting mainly. However, our understanding of thermal-quenching (TQ), i.e., the loss of photoluminescence (PL) intensity with increase of temperature, remains incomplete, with several competing theories. In this work, we demonstrate the application of *ab-initio* molecular dynamics (AIMD) simulations as a novel approach to investigate the effect of temperature on

Eu^{2+}/Ce^{3+} local environment (LE). A statistical analysis of the activator LE is extracted from the atomic trajectories from AIMD at multiple temperatures revealing a clear relationship between the temperature-dependent activator LE, and the experimentally measured TQ in numerous well-known phosphor compounds. We have found that phosphors with low TQ show a small variability in their activator's LE distribution within the operating temperature range. We propose a model where the activator LE fluctuations due to temperature lead to changes in the crystal field splitting around the activator, which in turn have a consequence on the photoionization barrier and TQ behavior. Finally, we propose structural descriptors based on these observations that can be used to rapidly screen novel materials for high quantum efficiency phosphors with excellent TQ resistance.

Chapter 1 Introduction

1.1 Background

Next-generation energy technologies are required to efficiently offer useful energy services (e.g., light, heat, mobility power, etc.)[1] Solid-state lighting (SSL) technology is a prime example of how energy can be converted into a useful service, namely lighting. Artificial light's increasing prominence consumed 6% of the total US energy and 15% of the total electricity consumed in the U.S in 2015.[2] However, LED lighting consumption in the U.S has a current annual primary energy savings estimated at 0.3 Quads (quadrillion British thermal units), equivalent to approximately 30 TWh/yr and $3B/yr in energy and cost savings.[2] SSL still has a considerable headroom for improvement in terms of efficacy and cost, and also has the potential to improve human performance and reduce physiological impacts currently experienced by legacy sources.[3] Figure 1.1[4] is a logistic fit to project the total lighting energy consumption over the next two decades, which eventually is expect to increase. If the U.S Department of Energy (DOE) targets are continuously met, SSL technology could save the U.S a total of 5.1 Quads of primary energy per year, equivalent to $50B/yr, which already accounts for 5% of the total U.S energy budget.

Presently, LED lighting packages are pre-dominantly built using three different architectures, the phosphor-converted LED (pc-LED) architecture, the hybrid LED (hy-LED), the color-mixed (cm) architecture. Pc-LED is usually made of a blue LED, which essentially pumps green and red wavelength from down-converters (e.g., phosphors). The hy-LED relies on a blue LED used to generate green wavelengths from downconverters, and a red LED is mixed with the green and blue light to produce white light. Finally, a cm architecture uses red, green blue and amber (RGBA) mixture to again produce white light.[2] The pc-LED architecture is the earliest and is the most dominant technology for white light production due to three major advantages. Pc-LED

require only the usage of one single type of LED device, and also provide high temperature robustness (e.g., indium gallium nitride (InGaN) blue LED), and phosphor downconverters can easily operate at elevated temperatures. Another advantage offered by pc-LED is the color stability and color tunability which can be determined during manufacture by controlling phosphor powders density and concentration, as well as LEs modifications around emission centers.[5]

Most phosphors are made of an inert host lattice usually forming a wide bandgap material (e.g. oxides, nitrides, sulfides, or oxynitrides) and a small amount of activator, typically one or two rare-earth or transition metal elements. It is a convention to write a phosphor composition as host:activator. As an example, the commercial blue phosphor $BaMgAl_{10}O_{17}$ (BAM) activated with Eu^{2+} is conventionally denoted as $BaMgAl_{10}O_{17}:Eu^{2+}$. It is essential to note the inherent difference between phosphors previously used for fluorescence and phosphors used for SSL applications. Florescent lamps are well established and known to have reached their physical limits[6]; however, phosphors for SSL applications are still being developed, especially for near-UV LEDs packaging. Activators play a crucial role in phosphor operation as they act as luminescent centers. Commonly used activators are lanthanides: $Eu^{2+}/Eu^{3+}/Ce^{3+}$ etc. Amongst all available rare-earths, only Ce^{3+} and Eu^{2+} offer emission at visible wavelengths, thus represent the only substantial possibility for white light creation *via* solid-state lighting. Hence, this thesis will solely reflect efforts on investigating Eu^{2+}/Ce^{3+} activated phosphors.

1.2 Pc-LED Architecture: Current Status and Opportunities

In the past decade, luminous efficacies of pc-LEDs have markedly increased, from less than 50 lm/W to approximately 150 lm/W as shown on Figure 1.2. On the one hand, pc-LED's increase in efficiency is predominantly due to the improvements made on blue LED chips - the science behind semiconductors is highly advanced and well-established. On the other hand,

although phosphors also have improved in terms of efficiency and emission spectra; the opto-electronics of phosphors are still not well-understood and theoretical shortfalls greatly inhibit phosphors development. A practical luminous efficacy of 255 lm/W is deemed possible for pc-LEDs – a factor of 1.6 beyond the current state-of-the-art pc-LED package. To understand the current status of the state-of-the-art pc-LED and the available opportunities, an estimated electricity-to-visible-light power-flow diagram for a current LED warm light is depicted on Figure 1.3.[2] A hypothetical 1 W is injected into the blue LED package (InGaN) and 137 lumens of white light emerges at the right, with an overall pc-LED package efficiency of 33%. The most commonly used blue LED has a 66% conversion efficiency and the hypothetical 1 W results into 0.66 W of blue optical power. The 34% losses are due to a combination of electrical resistance losses, non-radiative recombination of injected electrons and holes at low current density inducing a low internal quantum efficiency (IQE), or efficiency droop due to high current density (35 A/cm^2), and the high-index of InGaN results in an incomplete extraction of the generated blue light. [7-8] The green and red phosphors considered in the diagram convert the 0.66 W with a 63% efficiency into 0.035 W of blue, 0.087 W of green, and 0.294 W of red. The 37% loses this time are due to each phosphor's IQE, a large Stokes deficit due to the high energies of blue photons compared to green and red photons and mixing/scatter/absorption losses. The most important loss emanates from the Stokes efficiency loss where the red component shows a 25% loss, while the green and blue endure 15% and 0% loss, respectively. Moreover, the second most important loss contribution is the white light spectral efficiency loss (15%). The current full-width-half-maximum FWHM-wide (80 nm) of the red phosphor emission causes an important spillover of light into the deeper red, a region where the human eye is less sensitive to. A higher luminous efficacy of radiation (LER) can only

be improved through a selective control of spectral distribution of optical power, while the other losses mentioned earlier are not likely to be eliminated.

Based on the challenges facing pc-LED packages, several opportunities are presented in order to better its luminous efficacy. The red downconverter linewidth reduction is the most critical component inhibiting the enhancement of the current performances. It can be seen on Figure 1.4 that the relative LER can be increased with narrower red linewidth and a 95% relative LER can be achieved for a 35 nm FWHM. It is also important to not induce any penalty in color rendering quality while decreasing the linewidth of the red downconverter. Accordingly, the upcoming challenges in down-converting phosphors is to develop narrower emission linewidths, while maintaining a high IQE, a high thermal stability (TS) or low thermal quenching (TQ) temperature, and a centered red emission around 614 nm.

1.3 Essential Metrics for Phosphors

Several properties of phosphors are to be considered for practical applicability and are shown on Figure 1.5

1.3.1 Emission property

Depending on the requirements of each lighting applications, an appropriate emission spectrum is desired. Generally, human-centric lighting requires specific peak position, bandwidth and spectral distribution of phosphors' emission wavelength. The most commercialized white pc-LED is based on a combination of blue LED chips and yellow-emitting $Y_3Al_5O_{12}:Ce^{3+}$ ($YAG:Ce^{3+}$). The application range of such pc-LED package is limited by its cold white light (CCT < 8000K) and low color rendering index (CRI < 75) due to a lack of red-emission component in

the overall emission spectrum. High-quality and brightness LEDs ultimately require red phosphors with narrow-band character.

1.3.2 Excitation property

The excitability of phosphors is an important component for pc-LED packages as well. Commonly, UV chip and blue-chip emitting respectively at 355-400 and 440-460 nm are used as excitation sources for phosphors. Therefore, phosphors are required to have a strong broad-band absorption able to efficiently absorb photons from these LED chips. Moreover, reabsorption between excited and emitted photons is to be avoided in order to ensure high overall efficiency in the device.

1.3.3 Quantum Efficiency

Quantum efficiency (QE) is a measurement of the quantity of wavelengths of emitted photons from a phosphor material as a function of a known quantity of exciting photons. QE is usually determined experimentally through photoluminescence (PL) measurements at room temperature. When computing the optical output power of a phosphor, the external QE (EQE) is to be considered, where EQE is the ratio of emitted to incident photons at room temperature, including reflected photons. Internal QE (IQE) also referred as the phosphorescence quantum yield (QY), refers simply to the ratio of emitted to absorbed photons also measured at room temperature. IQE values over 90% are considered vital for commercialization.

1.3.4 Environment Stability

Commercialization of pc-LEDs requires a large device lifetime, where the color and intensity of phosphors should remain stable throughout its operation lifetime. Humidity also poses an important problem for phosphors application, i.e. $(Sr,Ba)_2SiO_4:Eu^{2+}$ or $(Ca,Sr)S:Eu^{2+}$ are

known to be moisture sensitive leading to irreversible optical degradation. It is always preferred to develop phosphor materials that are intrinsically resistive to humidity. Coating techniques forming protective layers on the surface are commonly developed. [9] Finally, it is important to note that color stability and lifetime expectancies vary among different commercialized products depending on their applications.

1.3.5 Thermal Stability

A current flowing through a conductor generates heat and in a LED package about 60% of the electrical input power is converted to heat leading to an increase of the LED package's temperature. An increase in the LED package, inherently affects the phosphor material causing a phenomenon known as thermal quenching (TQ). Experimentally observed, the emission peak of an activated host is broadened and decreased in intensity. TQ is measured by computing the ratio of an activated phosphor's IQE at 150℃ relative to its IQE at 25℃. Small TQ values are highly needed for practical applications. It is essential to note, that most of the heat generated by the pc-LED package is mainly centered aorund the phosphor, inducing the thermal quenching effect. While several coating techniques are permanently investigated, a theoretical undertanding and a prediction tool to thermal quenching are still a desirable appraoch to uncovering chemistries that are intrisically able to substain high temperature operation.

1.4 Features of Rare-Earth Ions with Respect to Luminescence

A brief introduction to the specific features of rare-earth ions is required before covering the main topic of thermal quenching predictions. Pc-LED's luminescence of phosphor materials is a multi-dimensional mechanism that can be explained via the configurational coordinate diagram (CCD), available electronic transitions in Eu^{2+}/Eu^{3+}/Ce^{3+}, energy transfer, sensitization of luminescence and concentration quenching of luminescence. For this study, it was assumed that

CCD and electronic transitions represent the core mechanisms required to explain thermal quenching.

Various models have been proposed to explain the presence and the absence of characteristic luminescence in phosphor materials; moreover, most of the proposed models are derived from the configurational-coordination diagram (CCD). An activator introduced into different lattices creates different luminescence spectra; more importantly, the absorption and emission positions are known to be different. The energy difference between the two positions is known as the Stokes shift. A CCD is a plot of the total energy U of the activator as a function of its configurational coordinates and offers a qualitative assessment of an activator's photoluminescence. The total energy is considered as the sum of the electron energy and ion energy for an isolated molecule. In fact, previous computational studies have found that the 4*f* states of Eu^{2+}/Ce^{3+} rare-earth dopants can have an atomic-like character as opposed to their bulk-like nature.[10] The total energy describing the bonding force between the activator and ligands can be expressed by Hooke's law, and the configurational coordinates are regarded as the average distance between the activator and the nearest neighbors. CCD has been widely used to explain Stokes shift, absorption/emission energy, and thermal quenching. However, current computational techniques are restrained to ground states calculations.

The Eu^{2+} and Ce^{3+} ions undergo electronic transitions between 4*f*-5*d* levels, where the ground state is denoted as $4f^{n}$, while the excited state is denoted as $4f^{n-1}$-$5d^{1}$. The 5^{d} energy splitting is strongly affected by the surrounding ligands, as explained by crystal field theory.[11] Essentially, crystal field theory describes the interactions amongst Eu^{2+}/Ce^{3+} and their surrounding ligands; electrostatic fields induced by the ligands and their geometrical symmetry have observable effects on the absorption and emission spectra of doped crystalline phosphors. The 5*d* orbitals

actively interact with their surrounding (crystal field strength). In fact, the geometry of the activator's polyhedron dictates the crystal field splitting of the 5*d* levels, and hence affects the 4*f*-5*d* transitions.[11]

1.5 Motivation and overview

Pc-LEDs for white light applications are expected to reach an efficacy of 226 lm/W by 2020, which requires further improvements. More essentially, the heat generated in the LED package affects both the lumen output and the lumen degradation and is mainly distributed in the phosphor layer. While thermal management of the down-conversion material layer is also a key research area, the understanding of the principal mechanism of thermal quenching is frustratingly limited. Moreover, current pc-LED packages are mainly derived from previous known phosphor compositions, and the process of novel phosphor discovery is highly driven by intuition and experience. However, numerous chemical spaces remain undiscovered and the development of a robust systematic screening is needed. Computational mining of unexplored chemistries for phosphors has shown a great potential to uncover phosphor hosts.[12] Despite several decades of extensive research efforts, our current understanding and prediction ability of the most crucial phosphor metrics remain qualitative. The goal of this thesis is to present a universal understanding of thermal quenching and develop a prediction tool to develop novel phosphor structures and compositions with targeted thermal stabilities.

This this thesis is divided into the following chapters:

Chapter 2 covers the *Ab-initio* Molecular Dynamics (AIMD) simulations conducted on 20 state-of-the-art phosphors. A thermal quenching prediction scheme is presented, where both LE rigidity and auto-ionization processes are utilized to explain the process of thermal quenching amongst

doped phosphor compounds. The study allows the development of structure-composition-property relationships in various phosphors and promises to be transferable to newer compositions.

Chapter 3 covers a detailed investigation of activators LE *via* a Voronoi Tessellation assessment of each's activator's polyhedron. In particular, a thermal quenching scheme solely based on 0 K intrinsic properties is developed and shows high accuracy for compounds mainly suffering from weak auto-ionization processes.

Chapter 4 summarizes the key findings in this thesis.

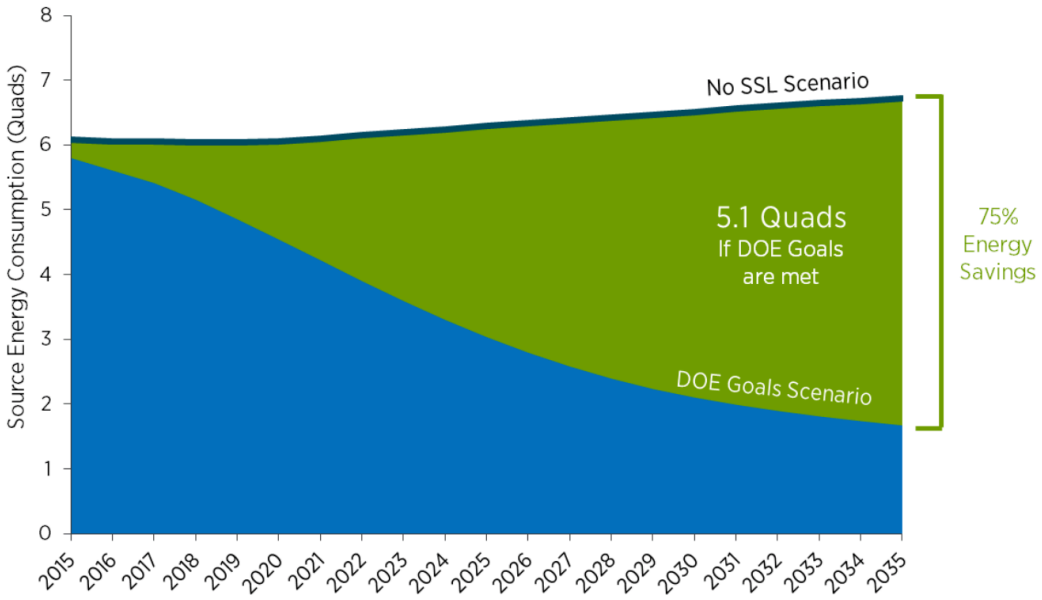

Figure 1.1 Department of Energy Solid-State Lighting Program Goal Annual energy saving forecast, 2015-2035

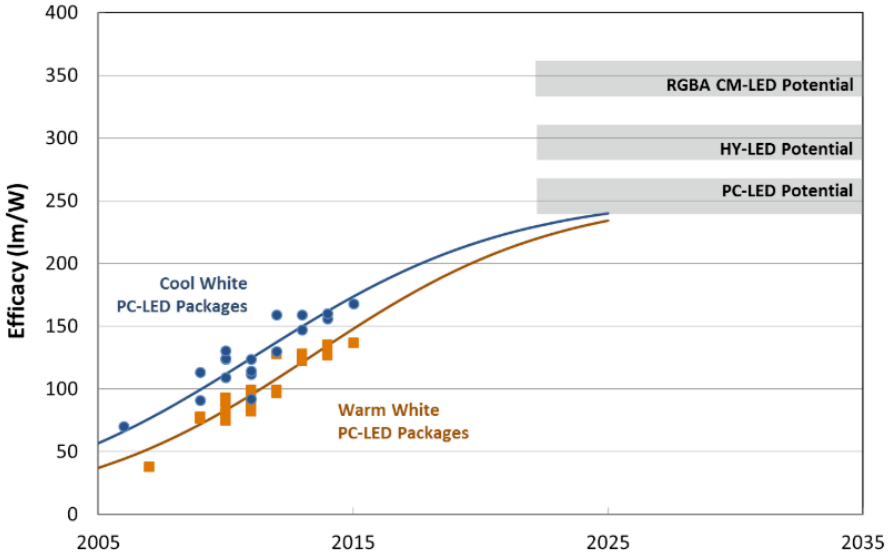

Figure 1.2 Efficacies of Commercial LED Packages measured at 25°C and 35 A/cm^2 input current density. Note, blue dots refer to cool white (5700 K), orange squares refer to warm white (3000 K), and the lines refer to logistic fit line.

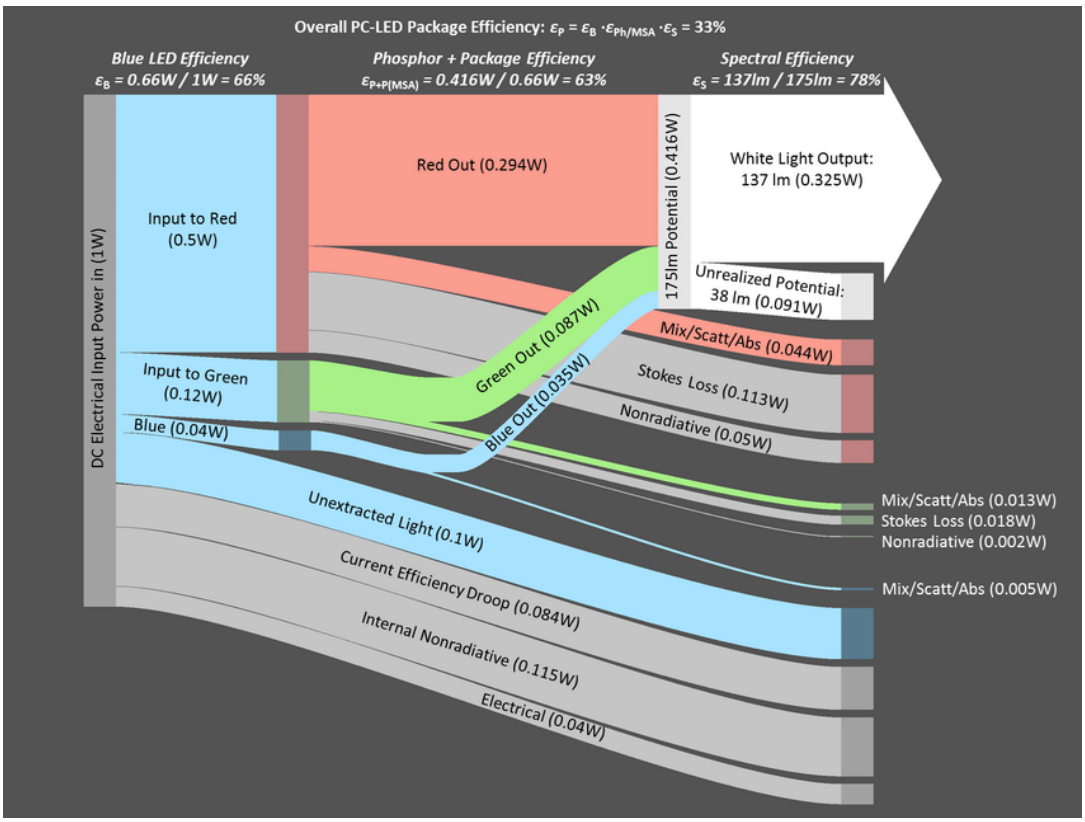

Figure 1.3 Electricity-to-visible-light power-flow-diagram for (state-of-the-art) warm white commercial pc-LED package.

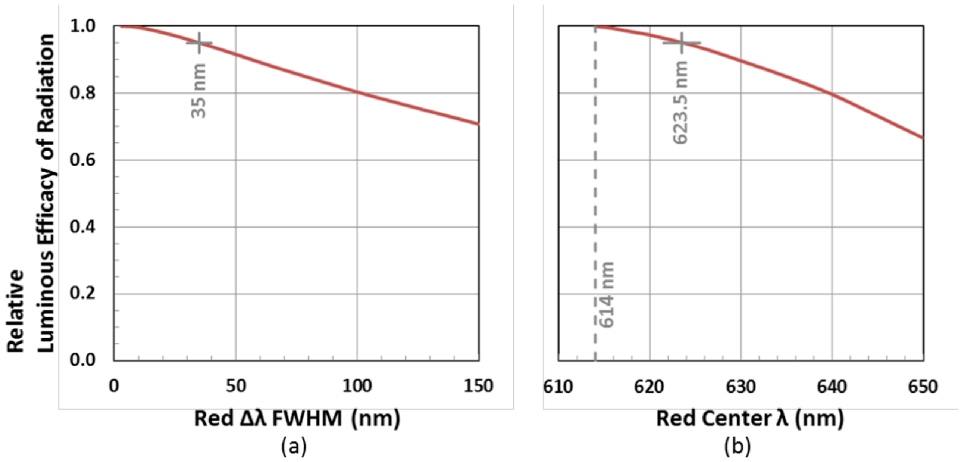

Figure 1.4 Relative White-light Luminous efficacy of radiation as a function of red light FWHM.

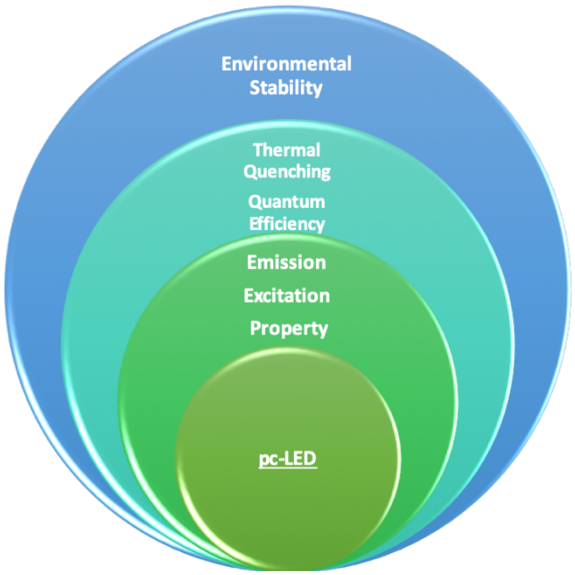

Figure 1.5 Import properties to be considered for pc-LEDs viability.

Chapter 2 *Ab-initio* Molecular Dynamics simulations on Phosphors

2.1 Introduction

Various properties are to be considered when addressing SSL devices' potential applicability in the market. Excellent candidates for SSL applications are required to have high quantum efficiency and high thermal stability. While scientists have thus far, a reasonable understanding on how to tune the absorption and emission spectrum of phosphors [13]; the tuning of thermal quenching remains an impalpable concept causing a consequential impasse for SSL development.

Throughout the last decades, several theories have been proposed to uncover the mechanism of thermal quenching in Eu^{2+} and Ce^{3+} activators phosphors; among which configuration coordinate diagrams were proposed to elaborate the temperature influence on the general process of absorption and emission *via* nonradiative routes. [14,15] A thermal mechanism formulated by Blasse and based on Jeffe's model argued that the emission's thermal quenching was ascribed to a large displacement (Δr) between the excited and ground states of Eu^{2+} in the configuration coordinate diagram. Moreover, Blasse and Brill have observed that Ba usually suffers from a higher quenching rate than Ca in isomorphous compounds when doped with Eu^{2+}.[16] While the observation is valuable, its applicability is not universal as Δr is only obtained *post-hoc*. Another work from Najavok suggests that thermal quenching could be assigned to a thermally driven release of a hole from Eu^{2+} $4f^6$ level to the valance band, which would cancel the coulombic interaction between the excited Eu^{2+} ($4f^6 5d^1$) electron and the Eu^{2+}($4f^6$) hole. This mechanism

was later discredited, since the thermal energy requires to release a hole from Eu^{2+} ($4f^7$) to the valance band is larger than the energy difference between the two levels.

Dorenbos devoted several of his work on re-evaluating the above proposed thermal quenching theories using high-resolution methods to estimate the absolute location of Eu^{2+} ground state $4f^6$ and excited state $4f^6 5d^1$ levels, and concluded that the mechanism for thermal quenching is ultimately correlated to the thermal excitation of the Eu^{2+} $4f^6 5d^1$ electron to the conduction band.[16] Dorenbos' results are consistent and offer valuable insights into the mechanism of Eu^{2+}/Ce^{3+} thermal quenching, suggesting the bandgap of the host material to be climacteric. However, these findings are not well-suited for a high-throughput screening whether a computational or an experimental one. In fact, computationally, the crystal field depression which is an essential parameter to computing Dorenbos' defined activation energy is difficult to calculate.

More recently, Brgoch et al. published a work which is more inclined to establishing a universal parameter to describing thermal quenching. The assumption that luminescent process of phosphors are highly correlated to their structural's intrinsic properties, allowed Brgoch's work to introduce DFT-calculated Debye temperatures as a structure rigidity descriptor of thermal quenching.[17] However, Jungmin et al, have shown exceptions to Brgoch's work.[18] In essence, structure rigidity is an essential metric in assessing the degree of structural changes a system can undergo at high temperatures; however, the local interaction between the host matrix and their respective activators is evidently not appraised yet. Moreover, the atomic-like behavior of activators requires the development of a local environment rigidity (LER) descriptor. *Grosso modo,* thermal quenching is essentially driven by the promotion of Eu^{2+} ($4f^6 5d^1$) electrons to the conduction band minimum (CBM), structural rigidity is an acceptable qualitative descriptor for hosts' thermal stability, but the current limitation of these models can only suggest that high

temperature optical behavior is of a much subtler characteristic. The most ubiquitous approach to comprehend temperature effects on activators and hosts is to utilize finite temperature *ab-initio* molecular dynamics (AIMD) simulations.

In this work, AIMD simulations under a canonical ensemble approximation are solely used to investigate the fluctuations of atomic positions, and hence incorporate a higher space resolution beyond the one-dimensional configuration coordinate proposed by Jeffe. Moreover, temperature effects on phosphors are inherently important, and thus far have never been computationally investigated. The use of advanced and robust local environment (LE) assessment techniques already implemented in pymatgen are used. [19] This innovative and *prima facie* instrumental perspective is an attempt to coalesce Jeffe, Dorenbos and Brgoch hypothesis into one singular model where the intrinsicality of host matrices on activators is appraised as one entity. Finally, the principal motivation of this work is not to only uncover the most correlated parameter to thermal stability, but to also enhance Wang's designed Workflow with an aim to discover new red phosphor materials. [20]

2.2 Methods

2.2.1 Structural relaxation of hosts.

All density functional theory (DFT) calculations were performed using the Vienna ab initio simulation package (VASP) within the projector-augmented wave method. [21,22] Perdew-Berke-Ernzerhof [23] (PBE) generalized gradient approximation (GGA) PBE functional for structure relaxations was used. The plane wave energy cutoff was 520 eV, and the Brillouin zones were integrated with a *k*-point grid density at least of 100 per $Å^{-3}$ (reciprocal lattice volume). Parameters conform to the Materials Project[24] were utilized to carry all properties calculations for host

materials, such as energy, and band structure calculations. Moreover, all crystal manipulations and data analysis were carried out by the use of Python Material Genomics[19] (pymatgen) package.

2.2.2 Structural relaxation of doped hosts.

For calculations of Eu^{2+}/Ce^{3+}-activated phosphors, we used the PBE+U method with a Hubbard U value of 2.5 eV.[10,25] Supercell models of at least 10 Å on each lattice parameter were adopted to simulate the low concentration of Eu^{2+}/Ce^{3+}-concentration in an experimental setting. Structures are entirely relaxed with energies and forces converged to within 10^{-5} eV and 0.01 eV $Å^{-1}$, respectively.

2.2.3 *Ab initio* Molecular Dynamics (AIMD) simulations.

Automated non-spin-polarized AIMD simulations were performed in an NVT ensemble at two temperatures 300 and 500 K with a Nose-Hoover thermostat.[26] A minimal Γ-centered $1 \times 1 \times 1$ *k*-point mesh and a time step of 2 fs were adopted. The simulation supercell sizes were at least 10 Å along each lattice direction.

2.2.4 Activator's LE (LE).

An advanced and robust LE (LE) assessment algorithm already implemented in pymatgen is used. The notion of Hoppe's effective coordination number (ECoN) is utilized to include a sense of bond weight based on geometry, leading to a chemically guided LE algorithm.[27] The use of ECoN was applied on 0 K structures in order to uncover the polyhedron geometry with the highest weight; consequently, a unique cut-off radius or maximum distance factor (MDF) is

selected and was then utilized to observe LE (LE) changes throughout AIMD simulations. MDF values are computed as follows:

$$MDF = \frac{B^X}{B^X_{min}},$$

where, B^X, and B^X_{min} are the ligand-activator bond length and the smallest activator-ligand bond length, respectively. While, ECoN values were computed as follows:

$$\boldsymbol{ECoN} = \sum \exp\left(1 - (\frac{B_i}{B_{abl}})^6\right), where\ B_{abl} = \frac{\sum(B_i \exp\left(1 - (\frac{B_i}{B_{min}})^6\right))}{\sum(\exp\left(1 - (\frac{B_i}{B_{min}})^6\right))}$$

$B_{i,}B_{min}, B_{abl}$ respectively are a ligand-activator bond weight, the lowest ligand-activator bond weight, and the average bond length weight.

2.2.5 Thermal quenching assessment from AIMD simulations.

AIMD trajectories are post-processed by succinctly computing the LE of Eu^{2+}/Ce^{3+} in activated host structures. More precisely, the coordination number (CN) at each AIMD timestep is recorded and inserted into a matrix

$$\mathrm{M} = \begin{bmatrix} CN_2 & \cdots & CN_{12} \\ \omega_{2;300} & \cdots & \omega_{12;300} \\ \omega_{2;500} & \cdots & \omega_{12;500} \end{bmatrix}$$

Note, all CN are computed using a unique set of geometrical parameters pre-defined from 0 K structural optimization. *M* intakes CNs from fluctuations at 300 and 500 K. After constructing the matrix *M,* a normalized Euclidean distance is computed as follows:

$$\mathbf{d_0} = \sqrt{\sum_{\boldsymbol{CN=2}}^{\mathbf{12}} (\omega_{CN;300} - \omega_{CN;500})^2} \qquad 2.1$$

$\mathbf{d_0}$ is ensured to be time-independent, rendering our observation true for virtually an infinite period. $\mathbf{d_0}$ is assumed to be a descriptor of LE rigidity (LER), and hence is an implicit descriptor of crystal field splitting perturbations. As will be explained later in the thesis, the use of $\mathbf{d_0}$ alone was not sufficient to achieve a high accuracy prediction and the use of PBE bandgap energies (E_g) as an electronic-property proxy enhances thermal quenching predictions from AIMD simulations. Essentially, PBE bandgap energies are assumed to be a proxy to auto-ionization processes and are utilized as follows:

$$\mathrm{TQ}(T_0) = \mathbf{d_0} \times e^{\left(\frac{AE_g+B}{KT_0}\right)} \qquad 2.2$$

T_0 is the target temperature at which the thermal quenching is to be predicted at, A is assumed to be an energy scaling factor, B is an energy correction term, and K is the Boltzmann constant. Equation 2.2 requires first to compute a value for $\mathbf{d_0}$ from AIMD simulations, and then a linear fitting is applied to solve for A and B. Moreover, PBE bandgap energies are input *via* an Arrhenius-like equation as emission intensities are expected to obey an Arrhenius trend where $\boldsymbol{d_0}$ is the pre-exponential term.

2.3 Results

2.3.1 Considered structures in this study

A total of 20 compounds are considered in this study, with two types of activators Eu^{2+} and Ce^{3+}. While only oxygen ligands are considered, a variety of unique geometries leading to different LEs are considered. In fact, the importance of activators' LEs with respect to their doped-host TQ will be divulged later. Table 2.1 comprises all considered compounds where an extensive range of TQ values is considered. Moreover, the structural, chemical and electronic diversity of the studied

compounds ensures that the developed understanding and prediction scheme can cover multiple structural lattices, PBE bandgap energies and hence offers high applicability.

2.3.2 Activator's CN: a weighted bond approach.

The analysis of AIMD trajectories heavily relies on investigating the atomic fluctuations endured by Eu^{2+}/Ce^{3+} activators at high temperature and requires a consistent and robust probe. Using Hoppe's ECoN has shown a substantial contribution on TQ predictions and is preferred over the conventionally defined CN, which is withheld from chemical and geometrical information that activator-ligands might intrinsically present. The notion of bond weight defined by Hoppe, allows to select ligands with the highest weight contribution and consequently ligands with the strongest effect on the activator's crystal field splitting are detected. Probing LEs behavior about their most contributing ligands have shown high correlation with TQ measurements. Figure 2.1 shows the discrete distributions of Eu^{2+}/Ce^{3+} CNs at 300 and 500 K for the 20 compounds presented in Table 2.1. Each of the 20 compounds was assigned a specific MDF value deduced from each structure's intrinsic geometry. In order to guarantee the consistency of the probe, MDF values are to be unchanged throughout AIMD steps and temperatures. In essence, MDF values were defined in order to ensure that only ligands with the highest weights are considered. It was observed that garnets structures such as $A_3Al_5O_{12}:Ce^{3+}$ (A=Y, Lu) experience minor changes in their CN distributions at 300 and 500 K; however, Eu^{2+} CN distributions in $Ba_2MgSi_2O_7$ or

Ba_2SiO_4 experience drastic changes. More importantly, the entropy of the CN distribution at one temperature is not correlated with the compounds' TQ.

2.3.3 Thermal Quenching Assessment from AIMD.

Activators' (Eu^{2+}/Ce^{3+}) LE fluctuations are interpreted as a discretized normal distribution of CNs at 300 and 500 K. Evaluating the difference between the two temperatures distributions is done by computing a Euclidean distance (Equation 2.1) and is assumed to be correlated to crystal field splitting changes around the activators. It is our working hypothesis that activator's LE fluctuations with respect to temperature implicitly lead to changes in the crystal field splitting, which in return have an effect on the auto-ionization barrier and TQ rate. It is, therefore, expected of TQ rates to be directly proportional to the computed Euclidean distances. Figure 2.2 shows TQ prediction results using the normalized Euclidean distance ($\mathbf{d_0}$). The R^2 value obtained from the linear fitting is of 0.58. The presence of outliers can first be explained by our initial attempt to reduce a high dimensional problem to a one-dimensional solution; by solely considering activators' LEs. $SrSc_2O_4$:Eu^{2+} is one of the outliers with the smallest bandgap energy within the considered compounds. $SrSc_2O_4$:Eu^{2+} has an experimental TQ value 98% and a computed $\mathbf{d_0}$ value of 0.087 while $BaLu_2Si_3O_{10}$:Ce^{3+} has an experimental TQ value of 30% and a computed $\mathbf{d_0}$ value of 0.093. The computed Euclidean distances are almost identical, although the TQ rates are very dissimilar. Nonetheless, $SrSc_2O_4$ host has a PBE bandgap energy of 3.426 eV and $BaLu_2Si_3O_{10}$ host has a PBE bandgap energy of 4.82 eV. Besides, $Sr_2Al_2SiO_7$:Eu^{2+} has a comparable experimental thermal quenching rate to Ba_2SiO_4 and Sr_2SiO_4, but somewhat smaller PBE bandgap energy than both compounds. Consequently, for an outlier (utilizing the Euclidean distance prediction) to exist within a set of compounds with comparable TQ values, a larger bandgap energy is required to compensate the over-estimation induced by $\mathbf{d_0}$. Inversely, a compound's TQ

prediction is under-estimated when its bandgap energy is smaller than other compounds with more-or-less similar $\mathbf{d_0}$ values.

The elaboration of a prediction scheme which includes information about bandgap energies is a desirable strategy to enhance TQ modeling. Equation 2.2 is proposed as an attempt to predict TQ for all oxides. Note that *A* and *B* are to be applied to all considered compounds (Table 2.1) and are expected to be transferable constants to novel and pre-existing compounds. Figure 2.3 shows the linear fitting obtained by applying Equation 2.2. It was found that including an Arrhenius-like fitting *via* PBE bandgap energies enhances the accuracy from 0.58 to 0.95. More importantly, the inclusion of an Arrhenius fitting only affected outliers; compounds outside of the confidence interval, while the trend remained mostly unchanged for predictions laying within the confidence interval.

2.4 Discussion

2.4.1 Detailed analysis of activator's LEs.

AIMD simulations were used to investigate a set of 20 compounds with a diverse range of structural and electronic properties. The set of compounds comprise 13 unique space groups including four different iso-structures: $Ba_9M_2Si_6O_{24}$(M=Lu,Y), $A_3Al_5O_{12}$(A=Y,Lu), M_2SiO_4(M=Ba,Sr), and $BaM_2Si_3O_{10}$(M=Lu,Sc).. Comparing iso-structures is insightful to comprehend the effect of atomic substitutions on structural behavior. The set of LEs introduced by the 20 compounds comprises 9 unique environments in terms of polyhedron geometry, which are depicted on Figure 2.4. More importantly, the 20 LEs considered in this study do not form a

clustered ensemble in terms of their geometrical features utilized to characterize them, e.g., environment types (cube, octahedron…), and average bond length, etc.

Moreover, this study heavily relies on the ability to rigorously compute the CN of Eu^{2+}/Ce^{3+} for various structures. However, the correctness of a CN is ambiguous and highly relative. Each structure offers Eu^{2+}/Ce^{3+} a unique set of LEs, with different bond lengths, and different bond lengths distributions. Some structures possess considerable variances in their bond lengths distributions resulting in a variety of possible LEs and CNs. Figure 2.5 reveals CNs and ECoN for Eu^{2+} or Ce^{3+} as a function of MDF. It is noted that for some structures, the computed CN is highly dependent on the MDF. The complexity of these LEs requires a careful selection of geometrical parameters ensuring that only the most relevant ligands are included within a well-defined shell. On Figure 2.5, we show with a grey-dashed line, the specific MDF values chosen for each of the 20 compounds.

Covering a wide range of LEs is also crucial for the development of a highly transferable TQ tool - photoluminscence properties of phosphors are intricately correlated to the activator's LE. In terms of electronic properties, all 20 compounds span a broad range of PBE bandgap energies ensuring the ability to correlate the effect of host PBE bandgap energies on TQ. Eventually, it can be argued that a set of 20 compounds investigated via AIMD simulations is not large enough to cover the multiplexity of thermal quenching processes; however, the uniqueness of each compound's characteristics offers a reliable route for developing a reliable TQ prediction tool. Furthermore, Ce^{3+} is known to have a blue-shifted emission compared to Eu^{2+} when inserted within the same host/environment, and theoretically are prone to suffer from a higher TQ rate – the lack thereof of Ce^{3+}-doped compounds having high TQ should induce a TQ under-estimation

for Ce^{3+}-doped compound with high thermal quenching. This will be covered in the following sections.

2.4.2 Probing technique of Eu^{2+} and Ce^{3+} LE from AIMD simulations.

The inorganic CN is well-known to have a versatile nature and infamously labeled as the 'inorganic Chameleon'.[27] Structural chemistry of short-range and long-range assembly in solid-state chemistry present an ambiguous definition for the CN which denotes the number of ligands arranged around a central particle in the first coordination sphere. Moreover, it is often customary in the SSL field to 'naively' define an activator's CN as a whole number matching the same CN as its host site. However, introducing an activator into a host lattice always has a long-range distortion effect on the lattice, leading ultimately to a distinct activator's LE from its host site. Therefore, a new labeling scheme solely based on the geometrical arrangement is highly needed to grasp the chemically induced geometrical distinctions. By assigning bond weights to every ligand/activator bond, ECoN can be assigned instead of the standard CN.

The choice of an MDF or cutoff radius can be arbitrary and has an immediate effect on the resulting ECoN. In this study, a combination of ECoN and MDF are utilized to define the most relevant LE around each activator rigorously. ECoN values are computed for a specific range of MDF values, and a specific value MDF value is chosen as the initial geometrical parameter to be used to process the displacements from AIMD simulations. It is essential for the MDF parameter to remain constant while processing all of the AIMD results. The screening of MDF values allow defining multiple LEs within a large enough coordination sphere. Eventually, ECoN values converge to a single value indicating that an increase in MDF does not lead to uncovering a new LE within the defined sphere. The mixture of Hoppe's effective CN and MDF screening allows defining a multi-weight ensemble of the LE, where every defined LE is also a multi-weighted bond

ensemble. Not only the highest weights bonds are included, but also the most relevant sphere of interaction is detected. Essentially, the optimized LE can be considered as the 3-dimensional center of gravity environment.

By doing so, it was found that for $Ba_9Lu_2Si_6O_{24}$, $BaZrSi_3O_9$, $BaLu_2Si_3O_{12}$, $Lu_3Al_5O_{12}$, $Y_3Al_5O_{12}$, $Ba_9Y_2Si_6O_{24}$, $SrSc_2O_4$, and $Ca_6BaP_4O_{17}$ defining the activator's LE is non-ambiguous due to bond lengths being virtually equal. For consistency purposes, we opted for an MDF value of 1.3 for such LEs. Other compounds offer different LEs depending on MDF values. For $BaSc_2Si_3O_{12}$, $KSrPO_4$, Sr_2LiAlO_4, $Ba_2MgSi_2O_7$, $CaMg(SiO_3)_2$ and Ba_2SiO_4 two possible CN are possible. For these structures, the effective CNs respectively were: 6.79, 7.83, 6.89, 7.22 6.81, 7.25 and 6.88 and suitable MDF values were respectively chosen to be: 1.3, 1.1, 1.2, 1.1, 1.2, 1.2, and 1.3. For the remaining oxides, $Sr_2Al_2SiO_7$, $SrMgAl_{10}O_{17}$, Sr_2SiO_4; $Ca_7Mg(SiO_4)_4$ and three possible CNs were possible, and the following MDF were respectively chosen: 1.2, 1.1, 1.2 and 1.2. These results are shown on Figure 2.5.

2.4.3 Thermal Quenching predictions.

Throughout high-temperature operation, activators and ligands endure small or large displacements suspected to be responsible, in parts; for their assigned thermal quenching. Experimentally, thermal quenching resistance is a measure of the emission intensity at 500 K relative to the emission intensity at 300 K; equivalently, assessing a doped host thermal quenching resistance requires the comparison of its activator's CNs at 300 and 500 K. Therefore, to compare the two discrete sets of CN, an n-dimensional Euclidean distance is computed. (Equation 2.1). However, the atomic fluctuations at both 300 and 500 K are only comparable if and only if they respectively occur at equilibrium state. While the total energy change can be used as a metric to evaluate the degree of equilibrium reached by our systems, it is also essential to confirm that

luminescent center's fluctuations throughout AIMD simulations are in a close-state of equilibrium. In this study, we will assume a system is at equilibrium when the Euclidean distance (Equation 2.1) is time-independent.

As shown in Figure 2.1, the discretized distribution of CN at 300 and 500 K is not *a priori* correlated to thermal quenching rates. Compounds showing a high entropy can also have a low thermal quenching and vice-versa. For example, $SrMgAl_{10}O_{17}:Eu^{2+}$ experiences CN changes from 2 to 6 while intrinsically it has a classical CN value of 9 and an ECoN value of 6.15. Obviously, the MDF of 1.1 is directly responsible for the high CN distribution entropy. However, despite drastic CN changes, $SrMgAl_{10}O_{17}:Eu^{2+}$ has a thermal quenching ranging from 12% to 5%. Understanding the primary mechanism behind $SrMgAl_{10}O_{17}:Eu^{2+}$ low thermal quenching necessitates a detailed investigation of Eu^{2+} LE. Using an MDF value of 1.4 will result on a computed CN value of 9 where the nine activator/ligands can be classified into four sub-neighbors: O1, O2, O3 and O4 with bond weights of 1.201, 0.839, 0.165 and 0.164 respectively. As reported in Table 2.2, the resultant vectors of O1, O2, O3 and O4 were computed and respectively labeled $\overrightarrow{\boldsymbol{V1}}$, $\overrightarrow{\boldsymbol{V2}}$, $\overrightarrow{\boldsymbol{V3}}$, and $\overrightarrow{\boldsymbol{V4}}$. It can be observed that $\overrightarrow{\boldsymbol{V1}}$ and $\overrightarrow{\boldsymbol{V2}}$ are aligned with the z-axis, while $\overrightarrow{\boldsymbol{V3}}$and $\overrightarrow{\boldsymbol{V4}}$ are mainly aligned with the y-axis with some minor orientation towards the z-axis. The resultant vectors unweighted, and weighted moduli were also computed. Weighted moduli were computed by considering each set bond weight. It was found that $\overrightarrow{\boldsymbol{V3}}$ and $\overrightarrow{\boldsymbol{V4}}$ will have a null resultant vector, while $\overrightarrow{\boldsymbol{V1}}$ and $\overrightarrow{\boldsymbol{V2}}$ will have a resultant vector pointing upward in the z-direction. Figure 2.6 (a) shows the repartition of oxygen ligands around Eu^{2+} in $SrMgAl_{10}O_{17}$, while Figure 2.6 (b-c) show $\overrightarrow{\boldsymbol{V1}}$, $\overrightarrow{\boldsymbol{V2}}$, $\overrightarrow{\boldsymbol{V3}}$, and $\overrightarrow{\boldsymbol{V4}}$ orientations as well as the weighted and unweighted moduli. Note, $\overrightarrow{\boldsymbol{V1}}$' is obtained by applying $1.20 \times \overrightarrow{\boldsymbol{V1}}$; 1.20 being the bond weight assigned to the O1 set. Intrinsically, the null effect created by $\overrightarrow{\boldsymbol{V3}}$ and $\overrightarrow{\boldsymbol{V4}}$ suggests that Eu^{2+} might possess oscillation

freedom in the y-direction, while the z-direction might impose a constrained oscillation to Eu^{2+}. Moreover, O3 and O4 bond weights are relatively small and suggest a lesser effect from those ligands. Bond orders based on atomic population analysis using DDEC6 between Eu^{2+} and O1, O2, O3 and O4 reveal in fact, that O3 and O4 sets have a bond-order of 0.0515; while O1 and O2 sets have a bond-order of 0.169 and 0.128 respectively. Lower bond-order values for O3 and O4 reflect a lower charge density and could reflect a low energy path explaining the observed mean-square displacements in Figure 2.7 (a-b). Mean-square displacements (MSD) results show a high correlation with the conclusions drawn from Eu^{2+} geometry and are shown in Figure 2.7 (a). MSD_y was observed to be the highest at both temperatures, while MSD_z are of an oscillatory nature as expected. Moreover, a Kernel density of the three MSD components at 300 and 500 K is plotted on Figure 2.7 (b). MSD_z are highly localized at 300 K, then undergo a broadening. MSD_x and MSD_y are dispersed and presumed responsible for the LEs' distribution changes from 300 to 500 K. It is believed that MSD_x and MSD_y are the principle reason behind the multiple TQ values found in literature. It is important to note that AIMD simulations apply a periodic boundary condition inherently simulating a long-range ordering, and suggests that long-ordering is required to create a minor oscillatory motion in the z-axis capable of preserving an intact LE distribution around O1 and O2 from 300 to 500 K. Based on these results it becomes evident that long-range ordering and high crystal quality is required to obtain a 5% thermal quenching rate. In order to better visualize the MSD behavior around Eu^{2+} in $SrMgAl_{10}O_{17}$ a 2-dimensional representation of the polyhedron at high temperature is illustrated in Figure 2.8 It is observed that O3 ligands have a higher MSD, while the O1 and O2 sets have a very similar behavior at 300 and 500K. Based on this analysis, it becomes understandable why a MDF of 1.1 was selected in order to probe the CN distribution throughout AIMD simulations. An MDF of 1.1 will ensure to detect the LE change in the 1^{st} sub-

shell, while a larger MDF value would have not been able to detect the minute changes within the 1st sub-shell. The same approach has been adopted for all other compounds. Moreover, the purpose of this detailed analysis is merely to introduce an intuitive understanding of ligands' intrinsic geometrical symmetry around an activator and their thermal fluctuation behavior.

While analyzing the particularity of other structures' atomic fluctuations is highly insightful in terms of understanding the effect of temperature on lattice vibrations, no quantitative correlations were found between the activator's displacements and their respective host thermal quenching properties. More importantly, investigating MSD behavior can only offer a qualitative way to predict thermal quenching. It is also important to note that low MSD behavior is not required to achieve low thermal quenching. Treating atomic displacements an as ensemble of CN distributions have showed to be a promising route to understanding the thermal quenching mechanism amongst the 20 compounds and is expected to be applicable to all phosphor compounds. Figure 2.2 are the results for thermal quenching rates predictions using the Euclidean distance defined previously, and the R^2 value was of 0.58. It was stated earlier that outliers represent a set of compounds whose bandgap energies were higher or lower than those having similar Euclidean distances. *De facto*, theoretically, if emission energies scaled proportionally to host bandgaps energies, and $\mathbf{d_0}$ was held as a constant, it can be speculated that host compounds with lower bandgaps energies are suspected of enduring higher thermal quenching rates, and *vice-versa.* Moreover, this speculation is well-observed within iso-structures of MF_2(M=Sr,Ca,Ba).[16] These results lead us to define $\mathbf{d_0}$ as a LE rigidity (LER) descriptor. Larger $\mathbf{d_0}$ values reflect LEs susceptible of larger variations under high-temperature operations, while smaller $\mathbf{d_0}$ values reflect LEs able to preserve their CN distribution and hence offer a relatively stable crystal field splitting. The LE rigidity and bandgap energies act as competing mechanisms in a non-linear fashion as

indicated by Equation 2.2 and the ability to model their effect has a great contribution on obtaining high-quality phosphors at targeted thermal stabilities. Moreover, it can safely be assumed that LER and auto-ionization are two independent events, vibrational and electronic ones. The probability of both events inducing thermal quenching can be modeled as a product function as defined in Equation 2.2. The second term in the right-hand side of Equation 2.2 is an Arrhenius fitting of PBE E_g and is an attempt to include auto-ionization contributions to LER. A and B terms are transferable constants to novel and pre-existing compounds and respectively were found to be: 0.043 and 0.40 eV. A is interpreted as a bandgap scaling factor, while B is an energy correction term and their linear combination with PBE E_g results in the activation energy endured by a compound with a specific $\mathbf{d_0}$ value. The model offered by Equation 2.2 reduces the high dimensionality of the thermal quenching problem to a two-parameter one. Thermal quenching predictions using Equation 2.2 are shown in Figure. 2.3.

To explain the mechanisms behind the model developed here, a reference to Blasse configurational coordinate is required.[15] The configuration coordinate diagram was derived based on the assumption that only ligands maintaining total symmetry around an activator contribute the most strongly to electronic properties.[15] In other words, the configuration coordinate diagram proposed by Blasse only depicts a singular LE around activators. However, our AIMD simulations have revealed that an activator possesses rather an ensemble of LEs, and the latter endures changes with temperature. It is then concluded that the ensemble of LEs recorded at a certain temperature reflects is a reflection of equivalent ensembles of configuration coordinates allowing our model to consider Blasse model quantitatively. Computing the Euclidean distance between two ensembles at two different temperatures is a measure of how shifted the electronic properties are from one temperature to another around an activator. Furthermore, auto-ionization processes as proposed by

Dorenbos are included by introducing an Arrhenius fitting of PBE E_g. Finally, our proposed model for thermal quenching is a product of an activator's local structure rigidity and an intrinsic electronic descriptor of the host. Prediction results from solely using the Euclidean distance are ultimately bettered by including PBE E_g. Prediction results from solely using the Euclidean distance are ultimately bettered by including PBE Eg. Moreover, the unbalance between the amount of Eu^{2+} and Ce^{3+} activated compounds, is expected to underestimate TQ values for Ce^{3+}-activated compounds; more precisely for compounds with small PBE Eg where the exponential rate is much higher. As mentioned earlier, Ce^{3+} characteristic emission is blue-shifted compared to Eu^{2+}. A different set of *A* and *B* parameters should be proposed for Eu^{2+} and Ce^{3+}. Two linear fittings were computed for each activator (Eu^{2+} and Ce^{3+}) by utilizing experimental thermal quenching results from an unpublished work, where Ce^{3+} is introduced into a host with a PBE band gap of 3.67 eV. As expected, the measured thermal quenching of the compound was of 95%. Figure 2.9 shows the results of thermal quenching predictions where two each activator is fitting separately. It can be observed that that Ce^{3+}-activated compounds are expected to endure a faster thermal quenching rate with a decrease of LE rigidity. Figure 2.10 shows the comparison between all the possible simulated thermal quenching where the LE rigidity and band gap energies are variables. These findings offer groundbreaking results in terms of red-oxide phosphor exploration. Prior results have shown that host PBE band gap energies and emission energies have a positive relation, suggesting that red-emitting phosphors usually possess smaller PBE bandgap energies. More precisely, it was suggested that hosts with PBE band gap energies ranging from 2 to 3.8 eV would tend to have a red-emission spectrum. Based on the simulated TQ values from Figure 2.10, a potentially red-emitting phosphor with thermal quenching values lower than 10% is required to

have a LER value lower or equal to 0.01. Therefore, a highly symmetric LE such as Ce^{3+} LE in $Y_3Al_5O_{12}$ is crucial to ensure a high LER and hence a small TQ.

2.5 Conclusion

In summary, we have demonstrated that the thermal quenching process is related to both structural rigidity and auto-ionization process. More fundamentally, the structural rigidity is of a localized nature - the ability for an activator to preserve an intact LE from 300 to 500 K is crucial for attaining a low thermal quenching rate. The LE rigidity denoted by $\boldsymbol{d_0}$ showed a reduced accuracy of 0.56, which was then explained by the lack of electronic properties information in our fitting. By introducing an Arrhenius-like equation which includes PBE bandgap energies, the process of auto-ionization was appraised and resulted in an accuracy of 0.96. The developed understanding of thermal quenching in this work provides an essential capability to predict thermal quenching behavior for computationally predicted structures, as well as understanding the primary mechanism behind each compound's thermal behavior. More essentially, the developed prediction scheme offers an unprecedented guidance unto red-emission oxides.

Table 2.1 Structure and Photoluminescence properties of some state-of-the-art phosphors.
Compounds, Space group, activators, intrinsic CN, effective coordination number (ECoN), continuous symmetry measure (CSM), average bond length (ABL), PBE bandgap energy (Eg), internal quantum efficiency at 25℃ Table 2.2 (IQE%), and thermal quenching resistance (TQR%) measured by the emission intensity or IQE at 150℃ relative to 25℃. The environment names (Env Name) stand for the following geometries: A:Cube, B:Octahedron, C:Square Anti-Prism, D:Trigonal Prism, E:Square-face bicapped antiprism, F:Square-face monocapped antiprism, G:Dodecahedron, H:Square-face bicapped trigonal prism, I:Trianguar Cupola

Compound	Space-group	Activator	Env Name*	CN	ECoN	CSM	ABL	E_g	TQ %	Refs
$Lu_3Al_5O_{12}$	$Ia\bar{3}d$	Ce^{3+}	A*	8	7.88	2.25	2.45	5.04	3	28–30
$Ba_9Lu_2Si_6O_{24}$	$R\bar{3}$	Ce^{3+}	B*	6	5.95	0.405	2.34	4.62	3	31
$Ba_9Y_2Si_6O_{24}$	$R\bar{3}$	Ce^{3+}	B*	6	5.95	0.315	2.34	4.51	20	32
$Y_3Al_5O_{12}$	$Ia\bar{3}d$	Ce^{3+}	A*	8	7.95	2.48	2.46	4.58	6	33–35
$Ca_3Sc_2Si_3O_{12}$	$Ia\bar{3}d$	Ce^{3+}	B*	6	6.00	0.0037	3.32	4.10	8-5	36–38
Sr_2LiAlO_4	$P2_1/m$	Eu^{2+}	F*	8	6.89	4.13	2.61	4.19	12	12
$Ba_2MgSi_2O_7$	$C2/c$	Eu^{2+}	B*	8	7.22	7.08	2.73	4.45	27	39
$BaLu_2Si_3O_{10}$	$P2_1/m$	Ce^{3+}	B*	8	5.82	5.24	2.65	4.82	30	40
$BaLu_2Si_3O_{10}$	$P2_1/m$	Eu^{2+}	H*	8	6.15	4.67	2.66	4.82	62	41
$BaSc_2Si_3O_{10}$	$P2_1/m$	Eu^{2+}	G*	8	6.79	6.68	2.67	4.73	25	41
Ba_2SiO_4	$Pmcm$	Eu^{2+}	F*	9	6.81	4.13	2.65	4.63	60	42
Sr_2SiO_4	$Pmcm$	Eu^{2+}	E*	8	5.07	4.11	2.57	4.38	63	42
$KSrPO_4$	Pm	Eu^{2+}	E*	9	7.83	2.82	2.67	5.10	13	43
$Ca_6BaP_4O_{17}$	$C2/m$	Eu^{2+}	G*	8	7.78	2.63	2.58	4.26	82	44
$Sr_2Al_2SiO_7$	$P\bar{4}2_1m$	Eu^{2+}	C*	8	6.31	2.24	2.60	4.0	50	45–47
$SrMgAl_{10}O_{17}$	$P6_3/mmc$	Eu^{2+}	I*	9	6.15	5.92	2.76	4.8	12-5	48,49
$SrSc_2O_4$	$Pnma$	Eu^{2+}	G*	8	7.65	1.01	2.60	3.4	95	50
$BaZrSi_3O_9$	$P\bar{6}2c$	Eu^{2+}	B*	6	6.00	5.13	2.69	4.68	22	51,52
$Ca_7Mg(SiO_4)_4$	$Pnn2$	Eu^{2+}	D*	6	4.5	13.04	2.58	4.18	60	53
$CaMgSi_2O_6$	$Pmcm$	Eu^{2+}	C*	8	7.25	2.54	2.70	4.55	75	53

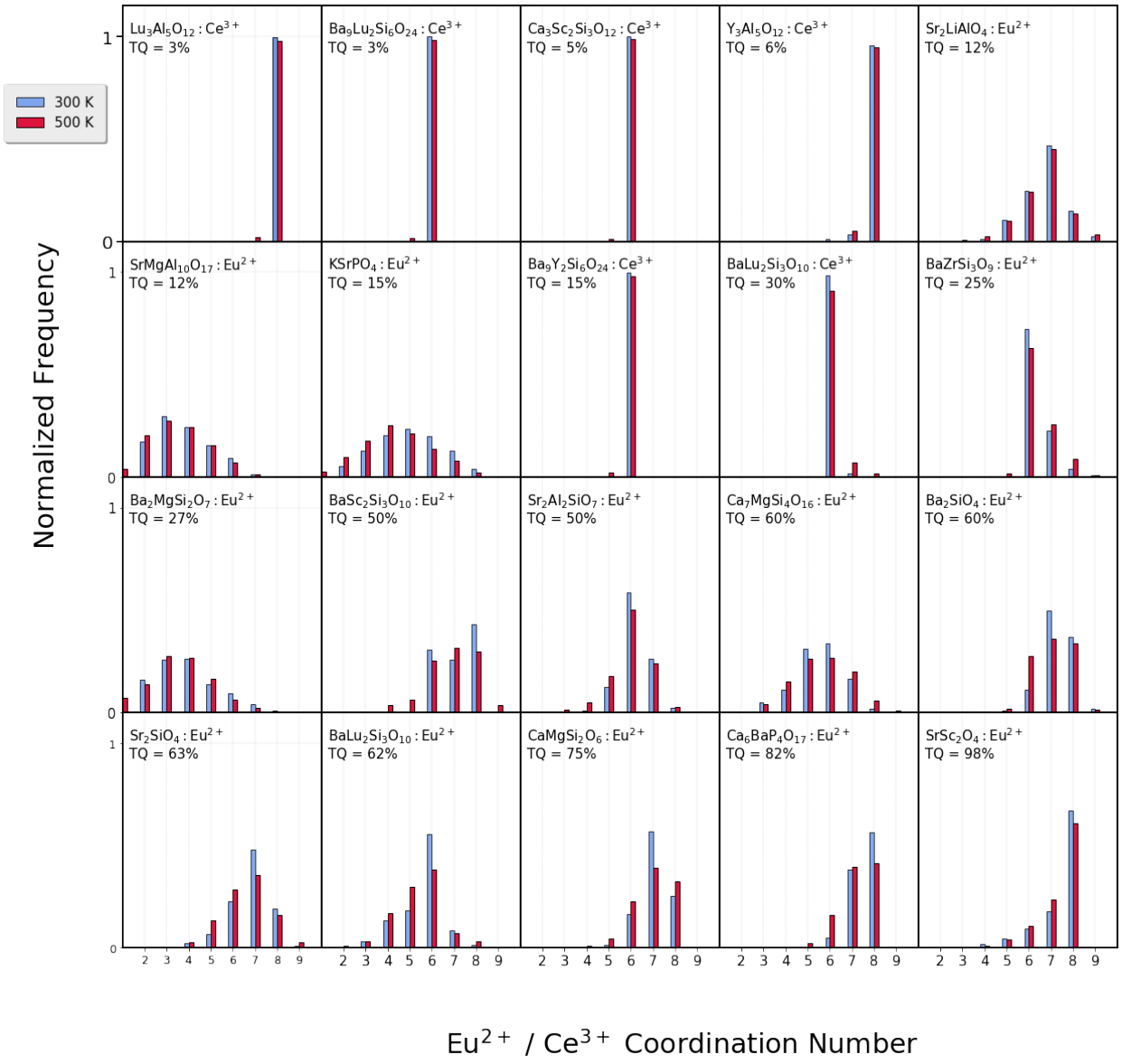

Figure 2.1 The distribution of Eu^{2+}/Ce^{3+} CN at 300 and 500 K from AIMD simulations for all 20 compounds presented in Table 1.

Experimental thermal quenching data is summarized in Table 1 as well. It can be observed that compounds with low thermal quenching experience minor changes in their CN distribution; however, Eu^{2+} doped in $SrMgAl_{10}O_{17}$ endures substantial LE changes yet has a low thermal quenching rate. It is also important to note that CNs' entropy is not correlated to thermal quenching resistance. Thermal quenching rates are ordered in an ascending fashion.

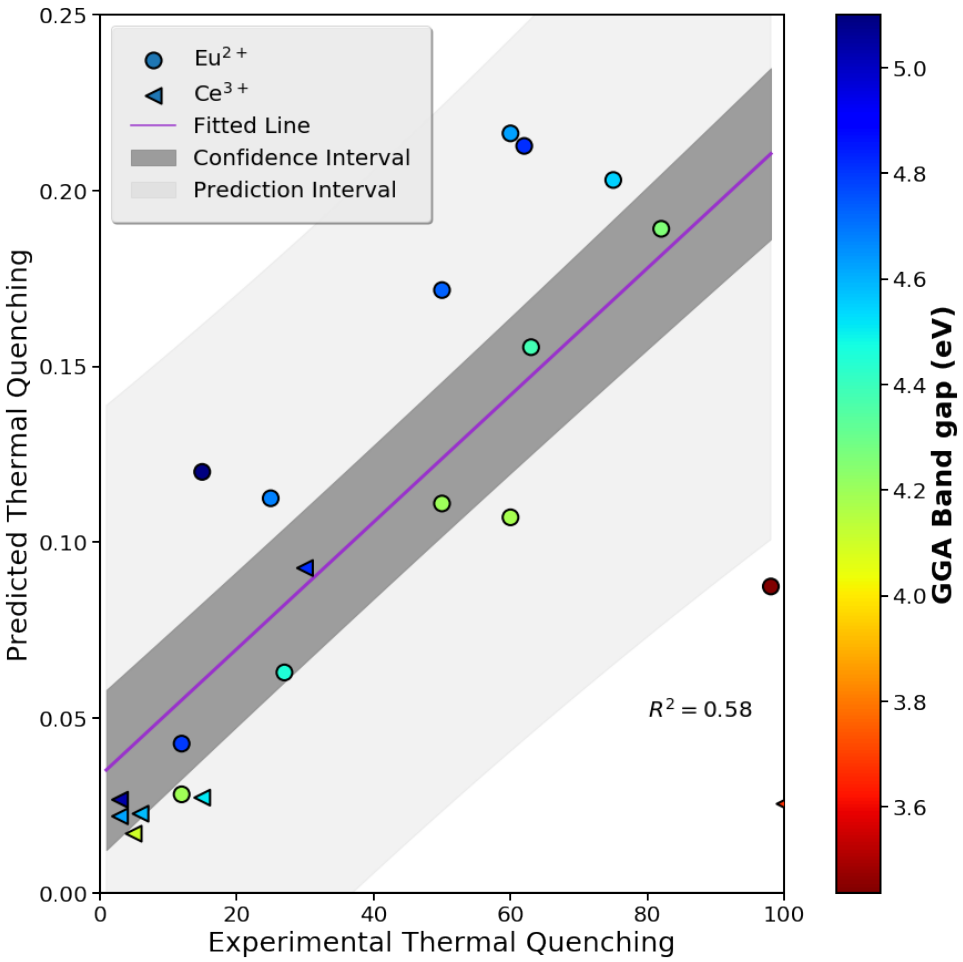

Figure 2.2 Predicted TQ using Equation 2.1 versus Experimental thermal quenching.
Predicted TQ values are the Euclidean distances computed by Equation 2.1, following an ordinary Euclidean algorithm of 11-dimensions; each dimension reflects a specific CN. The dimension of the Euclidean distance is purposely defined as to cover all possible CNs from AIMD simulations. The normalization of the Euclidean space ensures consistency and comparability within the computed values. The R-squared value of the linear fitting is 0.57. The low accuracy of the prediction is due to the presence of outliers which posteriorly is linked to the wide range of bandgap energies in the 20 set of compounds.

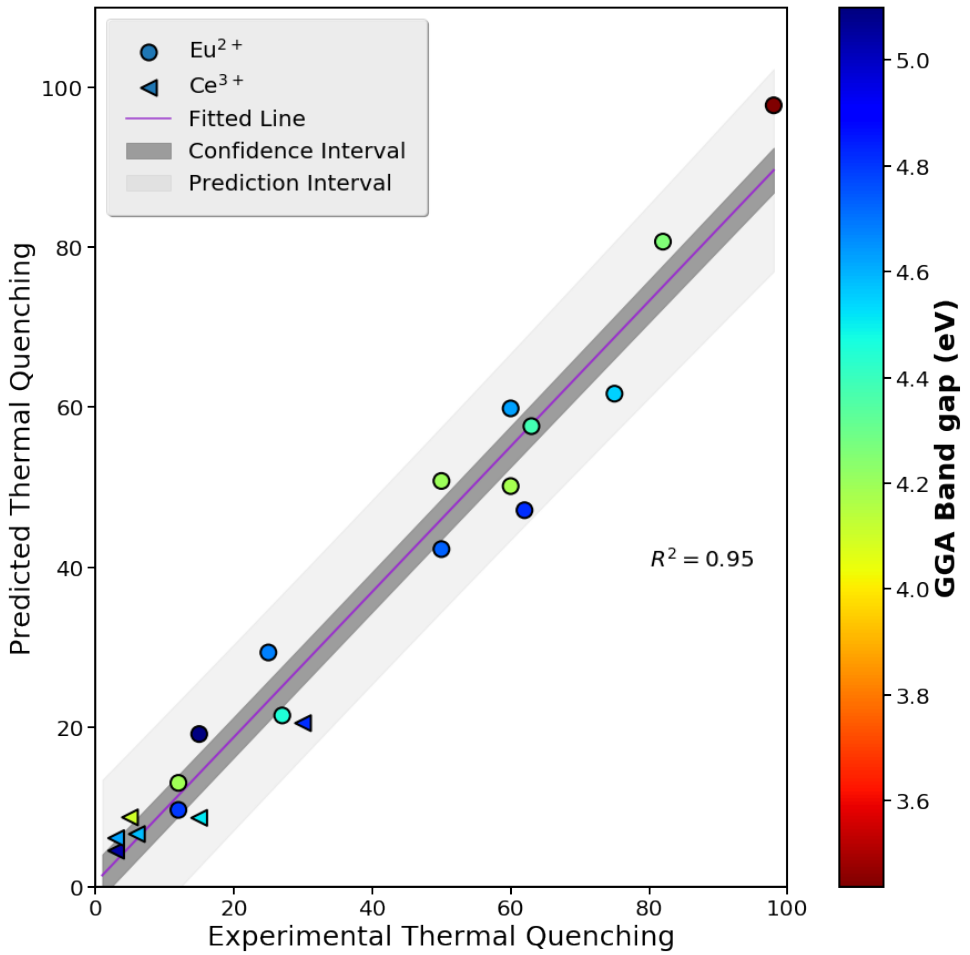

Figure 2.3 Predicted TQ using Equation 2.2 versus Experimental TQ.
Thermal quenching predictions were computed by Equation 2.2, where bandgap energies were fitted into an Arrhenius like equation. The R-squared value of the linear fitting is 0.96 reflecting a higher prediction accuracy than the previous fitting computed by Equation 2.1.

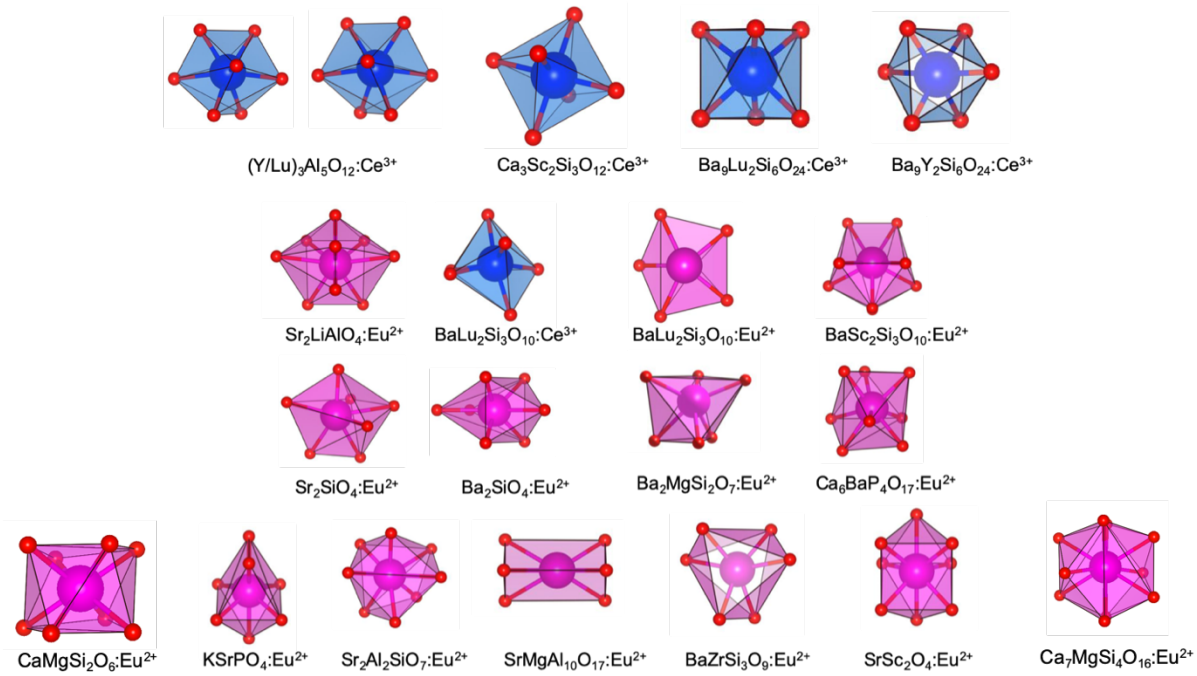

Figure 2.4 Eu^{2+}/Ce^{3+} LEs for the 20 compounds present in Table 2.1.

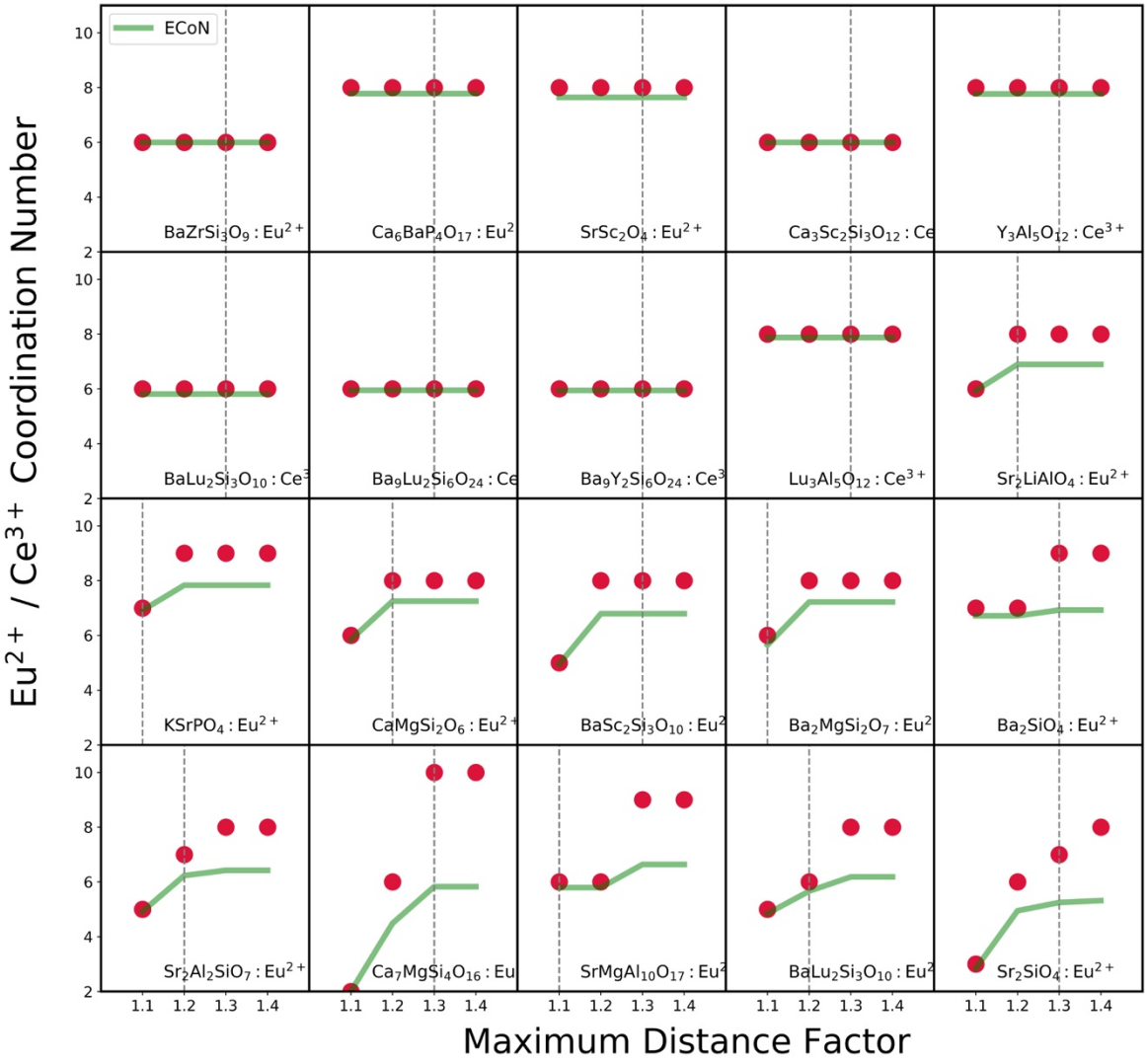

Figure 2.5 Computed CNs as a function of maximum distance factor (MDF).
The computed CN is highly dependent on the MDF parameter. The gray dashed line shows the select MDF parameters in order to probe the AIMD displacements of Eu^{2+} and Ce^{3+}.

Table 2.3 Detailed information on O1, O2, O3, O4 ligand sets in $SrMgAl_{10}O_{17}$.
Note, the $\overrightarrow{\boldsymbol{V1}}$, $\overrightarrow{\boldsymbol{V2}}$, $\overrightarrow{\boldsymbol{V3}}$ and $\overrightarrow{\boldsymbol{V4}}$ vector coordinates are within the crystallographic frame. Moreover, weighted vector coordinates are computed by taking the product of bond-weight and unweighted vector coordinates.

	BOND LENGTH (Å)	**BOND WEIGHT**	**WEIGHTED VECTOR COORDINATES**
O1	2.672	1.20	$\overrightarrow{V1} = [0,0,\mathbf{7.78}]$
O2	2.836	0.85	$\overrightarrow{V2} = [0,0,-\mathbf{5.98}]$
O3	3.284	0.164	$\overrightarrow{V3} = [0,-\mathbf{0.54},-0.024]$
O4	3.285	0.165	$\overrightarrow{V4} = [0,-\mathbf{0.56},0,-0.012]$

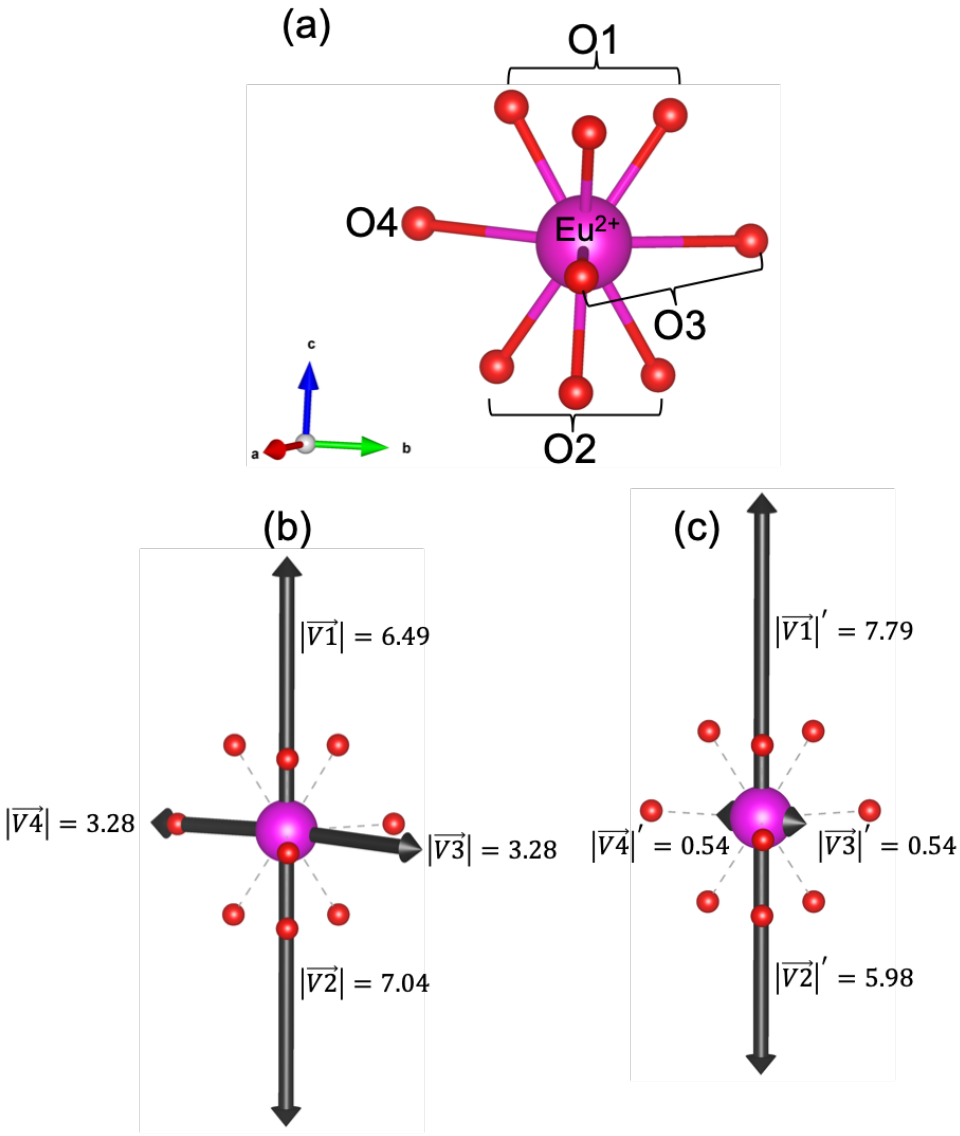

Figure 2.6 (a) Eu^{2+} full LE with a maximum distance factor of 1.4 in $SrMgAl_{10}O_{17}$.
The continuous symmetry measure value is 15.34 reflecting a highly distorted LE. O1 represents the closest set of oxygen ligands with a bond length of 2.672 Å – these ligands form the first sub-shell. O2 represents the second closest set of oxygen ligands with a bond length of 2.836 Å – the three ligands form the second sub-shell. O3 and O4 and the three furthest set of oxygen ligands with a bond length of 3.284 Å. The ECoN is of 6.6, suggesting that O1 and O2 have the highest coordination weight. (b) $\overrightarrow{\boldsymbol{V1}}$, $\overrightarrow{\boldsymbol{V2}}$, $\overrightarrow{\boldsymbol{V3}}$, and $\overrightarrow{\boldsymbol{V4}}$ the resulting vectors from O1, O2, O3 and O4 ligands, respectively. (c) The Bond weight of each set of ligands is multiplied their respective vectors in order to take into consideration the weight of each set and resulting on new vectors: $\overrightarrow{\boldsymbol{V1}}'$, $\overrightarrow{\boldsymbol{V2}}'$, $\overrightarrow{\boldsymbol{V3}}'$, and $\overrightarrow{\boldsymbol{V4}}'$.

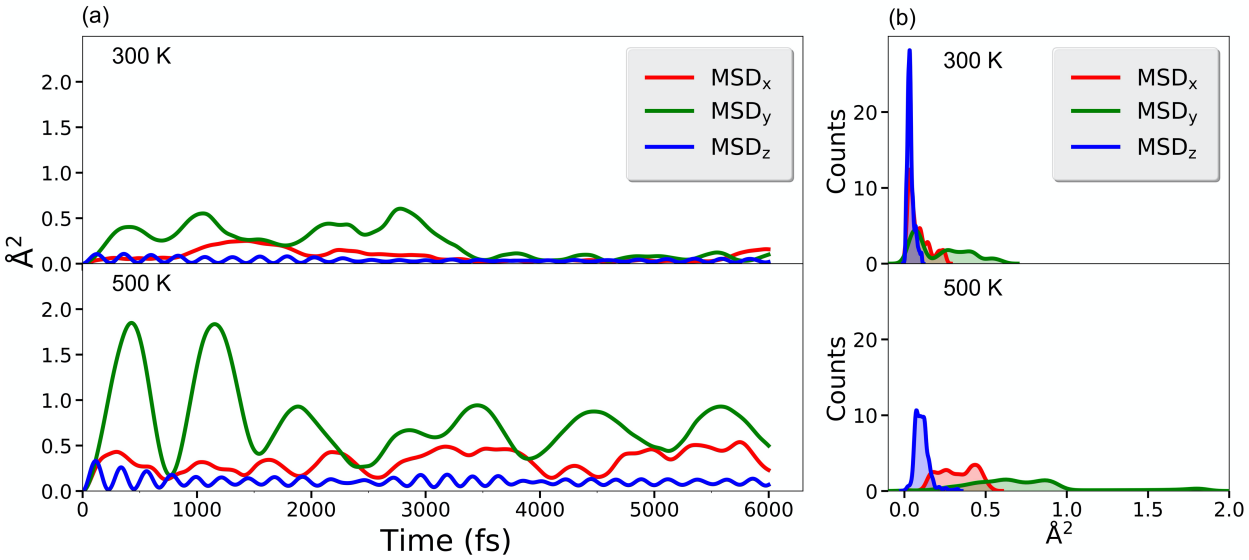

Figure 2.7 (a) Mean-square displacements components (MSDx, MSDy, and MSDz) of Eu_{2+} doped in $SrMgAl_{10}O_{17}$ at 300 and 500 K.
(b) Kernel density plot of the mean-square displacements components at 300 and 500 K.

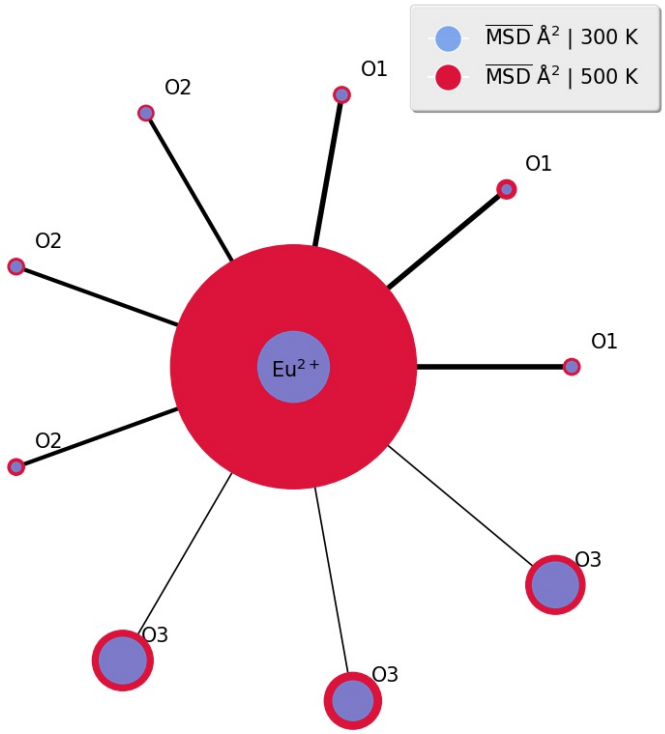

Figure 2.8 A 2-dimensional representation of Eu^{2+} LE in $SrMgAl_{10}O_{17}$, decorated with MSD mean values at 300 and 500 K.

The size of $\overline{\mathbf{MSD}}$ bubbles is used to compare the relative amount of mean-square displacements endured by O1, O2, O3 and O3 set of ligands and Eu^{2+}. Note, the thickness of the bond is directly proportional to each activator/ligand bond-order.

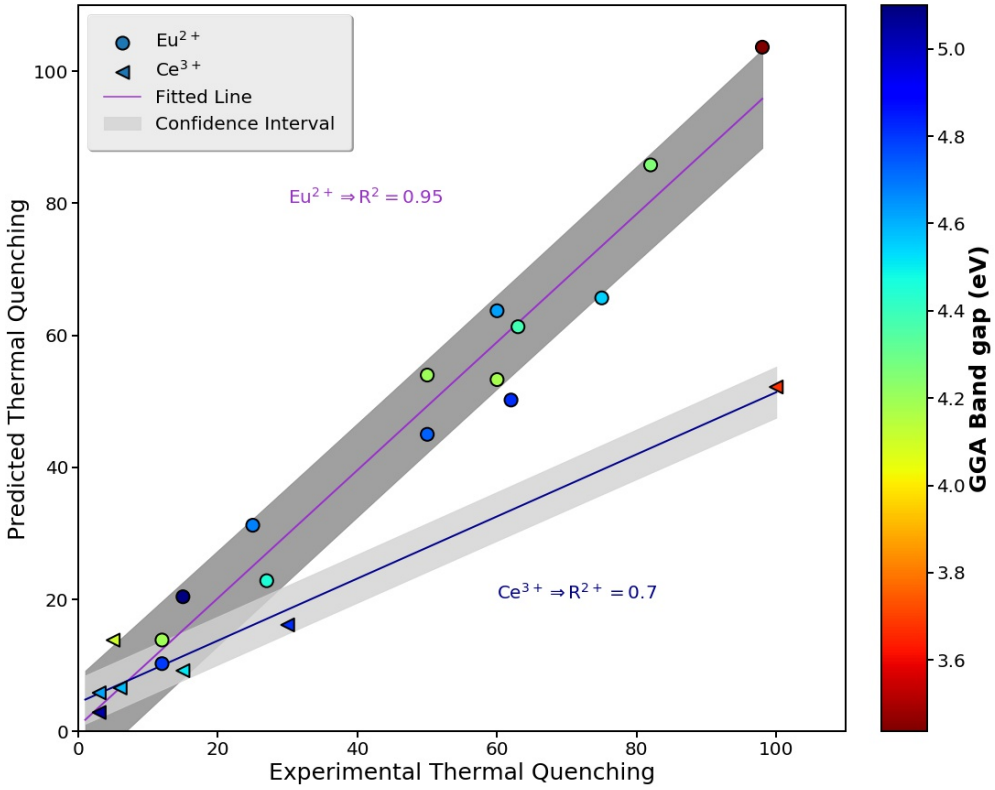

Figure 2.9 Predicted TQ using Equation 2.2 versus Experimental TQ.
Thermal quenching predictions were computed by Equation 2.2, where bandgap energies were fitted into an Arrhenius like equation. Two liner fittings are computed, one for Eu^{2+} and one for Ce^{3+}.

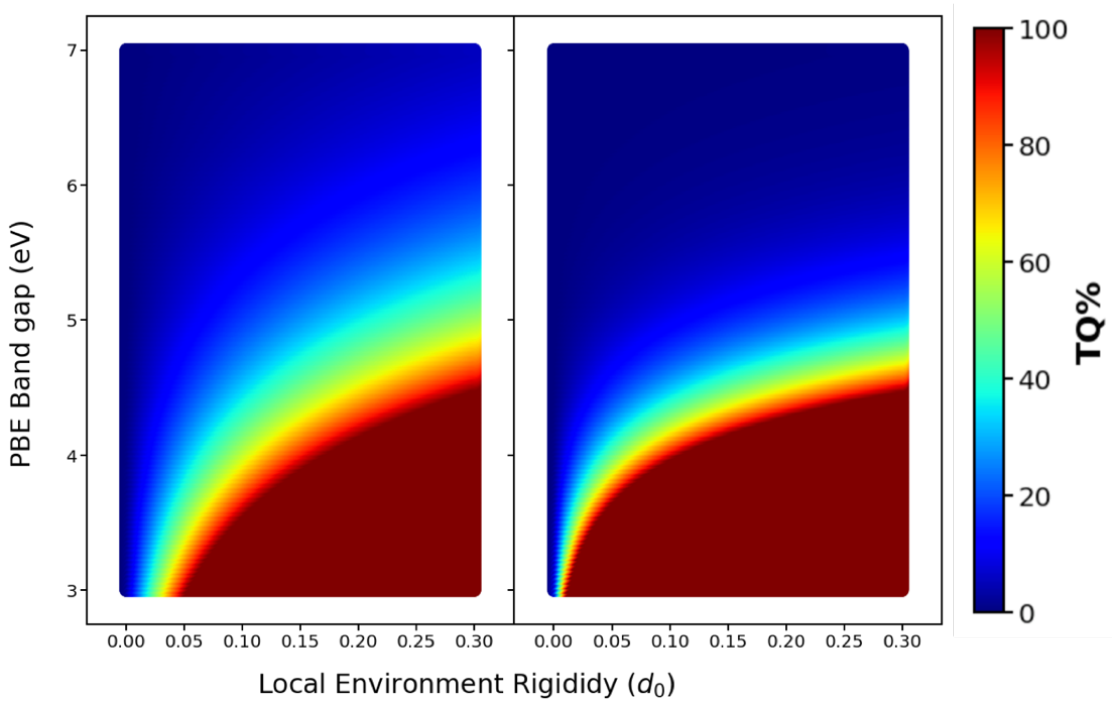

Figure 2.10. TQ simulated predictions as a function of different LE rigidity and PBE band gap energies for Eu^{2+} (left) and Ce^{3+} (right).

Chapter 3 Thermal Quenching predictions from 0 K geometries via LE Tessellations

3.1 Introduction

Classical chemistry has seen a central particle surrounded by ligands as a static entity cataloged with a single ‘naïve' CN. One of the greatest impediments in coordination chemistry is its inability to define accurately and distinctively a coordination environment. Pioneering work during the early 20's introduced the use of ionic or atomic radius and bond angle, which have come into use for the description and interpretation of crystal structure. [54] However, a century later, the scientific community mainly still relies on these simple tools; more importantly, the solid-state lighting community is bereft of a peculiar coordination environment assessment. While AIMD simulations results reveal the pertinence of assessing CNs as space-time entity, a substantial amount of computational resources is however required to conduct screening on all existing and predicted structures. Implementing a robust LE assessment to intrinsically investigate the intrinsic effects of luminescent centers environment is of the essence.

O'Keeffe proposed the concept that a central atom forms a Voronoi polyhedron where a weighted contribution of neighboring atoms correlates in proportion to the solid angle subtended by the face at the center. [54] Nevertheless, when probing luminescent centers in pc-LEDs, hindrance arises due to the lower symmetrical environments when polyanionic environments generate different interatomic distances. Recently Waroquiers et al.[55] revisited the O'Keeffe definition of CN environments and introduced a probabilistic distribution of coordination environments insensitive to small distortions in the structure. The probabilistic distribution algorithm represents one of the first practical attempts to formulating a global joint within properties and structures of materials. Furthermore, Mark Pinsky et al. developed a quantitative algorithm to evaluate the degree of any symmetry within any polyhedron.[56] The algorithm offers an effectual advantage

when dealing with luminescent centers in pc-LEDs by providing the latter a dynamic spatial capability. The continuous symmetry measure (CSM) as defined by Pinsky allows comparing distortion amongst all polyhedron even of different CNs, or ligands. In this chapter, we will substantially improve our DFT screening descriptors using insights from the Chapter 2. For example, the computed Debye temperature of the phosphor host crystal was initially used as a relatively crude descriptor for quantum efficiency and thermal quenching stability in previous DFT-based screening.[12,57] A drawn hypothesis from the Voronoi grid representation revolves around bridging Voronoi grid's area to the insights acquired from AIMD simulations, where the Voronoi grid is presented as an improved descriptor that shows better correlation with thermal quenching stability.

3.2 Methods

Waroquiers 's definition of a probabilistic LE distribution remains sustainable for minor distortions; a more substantial spatial screening is required to grasp most of the fluctuations a luminescent center endures at high temperature. Waroquiers's work defines two parameters, the distance parameter, and the angle parameter. The latter ones are commonly known as the radial distance from the origin (luminescent center) to ligands or the maximum distance factor (MDF), and the polar angle respectively in a polar coordinate system. Each coordinate system offers distinctive rules mapping pairs of numbers consistently to points in a plane. In a polar coordinates system, r and θ are evidently of different natures. One particularity of the polar coordinate is two different polar coordinates can map to the same point, due to the angle parameter modulus. This particularity is responsible for the uniqueness of polar coordinates where the angle parameter is constrained between 0 and 360. Coextensively, a Voronoi polyhedron projection requires a strict interval definition for both the angle and distance parameter. The distance parameter suitably

obeys classical chemistry fundamentals defining anionic ligands, and the angle parameter is defined to ensure the uniqueness of the mapped ligands.

A Voronoi representation computes a polar transformation of an activator's nearest neighbors into a cartesian frame. There exist two indispensable parameters to compute a Voronoi area:

$$\alpha = \frac{R^X}{R^X_{min}}$$

$$\gamma = \frac{\Omega^X}{\Omega^X_{max}}$$

R^X_{min}, R^X, Ω^X_{max}, and Ω^X are respectively the smallest radial distance between the central atom and all possible ligands, the distance at which the LE is considered, the widest angle allowed to preserve the uniqueness of the ligand set, and the angle at which the LE is considered. By screening multiple distances and angles at which a LE can be computed a two-dimensional map is constructed. The latter is a two-dimensional projection of a polyhedron and is plotted in Figure 3.1.

The Voronoi grid representation offers a remarkable and groundbreaking insight into an activator's LE. The Voronoi tessellation being, in theory, a polar curve can be further decorated by each CN's area. A polar transformation of the volume occupied by a LE is defined by Equation 3.1. The latter offers a robust way to compare the spatial contribution of CNs within different

structures, despite having different bond lengths. In terms of methodology, the Voronoi tessellation area is computed for CNs around the effective CN, and each grid's area is computed as follows:

$$\text{Area(CN)\%} = \frac{\text{Distance Factor}\times\text{Angle Factor}}{\text{Total Voronoi Grid Surface}} = \frac{\left|\frac{R_1-R_2}{R_{min}}\right|\times\left|\frac{\theta_1-\theta_2}{\theta_{max}}\right|}{\left|\frac{R_{max}-R_{min}}{R_{min}}\right|\times\left|\frac{\theta_{max}-\theta_{min}}{\theta_{max}}\right|} = \frac{|R_1-R_2|\times|\theta_1-\theta_2|}{|R_{max}-R_{min}|\times|\theta_{max}-\theta_{min}|}$$

(3.1)

Figure 3.1 shows an example of a Voronoi grid surface for Eu^{2+} doped in Sr_2SiO_4 host. For each angle and distance parameter range, a specific and unique CN exists. Moreover, the area of each CN grid can be computed by using Equation 3. Using the same approach to analyze the changes of CN during thermal fluctuations, the Voronoi grid area is to be calculated only around ECoN; the latter included as well. For example, Eu^{2+} in Sr_2SiO_4 has an ECoN of 5.32 making these geometrical parameters the center of gravity of the highest weight LE.

3.3 Results

A total of 29 compounds including the 20 compounds previously studied *via* AIMD simulations is utilized to predict thermal quenching values - both Ce^{3+} and Eu^{2+} activators are included. As explained in the Method section 3.2, a Voronoi area is computed around at most three CNs, where the central CN is the ECoN. It is found that the total area of the LEs has a positive correlation with thermal quenching resistances.

The Voronoi area as defined previously is computed for a total of 29 compounds, and the results are shown in Figure 3.2. A list of the 29 compounds is given in the Table 3.1. The accuracy of the linear fitting between experimental TQ and predicted TQ *via* Voronoi area has an R^2 value of 0.92. Moreover, the ability of the Voronoi area to correctly predict TQ, suggests that the Voronoi area should have a positive correlation with the AIMD results. Figure 3.3 is a plot of the pre-defined Voronoi area versus the results from Eq. 2 for the 20 compounds shown in Table 1. A

linear fitting was again computed with an R^2 value of 0.93. These results will be discussed in detail in the Discussion section, and a hypothesis will be given in order to explain such trends.

3.4 Discussion

AIMD simulations results provided insightful knowledge on phosphor operation at high temperature. The preservation of the LE's distribution from 300 to 500 K was a significant contributor to achieve low thermal quenching. Theoretically, fluctuations at 500 K include vibrational modes that are not necessarily present at 300 K or at higher amplitude. It can be assumed that for more significant deviation (larger $\mathbf{d_0}$ values), higher and additional vibrational modes are attained. Taking a closer look at the CN distribution on Figure 2.1 all of the 500 K distributions have a higher entropy reflecting the creation of new vibrational modes. Most importantly, the distributions at both temperatures are all centered around the same CN. Each box within the Voronoi Tessellation (Figure 3.1) is essentially a space volume where the activator and ligands have the freedom to move and preserve their CN. At high operation, some of the ligands might move from one box to another and generate new coordination as seen in Figure 2.1. Hypothetically, the amount of space available for a particular LE with a specific ligands' configuration can be regarded as a measure of its dynamic stability. In theory, the first-shell defined by a standard LE assessment can be stratified into several sub-shells. Each box defined by the Voronoi Tessellation visualization can be interpreted as a sub-shell. Each sub-shell is prompt to interactions from other sub-shells. The larger the area of the sub-shell the weaker the co-interactions are expected to be. These sub-shells co-interactions can easily be verified by computing the respective bond-order of each ligand.

Moreover, the Euclidean distance has shown to be a core component to thermal quenching predictions. Inspired from the physical meaning behind $\mathbf{d_0}$, we further developed a tool able to

intrinsically assess the dynamic stability of a LE by computing its projected 2-dimensional area. However, it should be noted that this tool is deemed to fail for compounds ought to suffer from a high auto-ionization process, mainly compounds with small PBE E_g energies, i.e., $K_3YSi_2O_7$ or $SrSc_2O_4$. Both compounds suffer from thermal quenching values higher than 95% at 500K. It should be noted that for $K_3YSi_2O_7$ and $SrSc_2O_4$ the Voronoi area for both Eu^{2+} and Ce^{3+} suggested a low thermal quenching. Auto-ionization becomes a critical component of thermal quenching when bandgap energies of host materials are relatively small, which explains the complexity of discovering a deep red phosphor with low thermal quenching.

In fact, it was found that the Voronoi area is directly correlated to the results from Equation 2.2; omitting $SrSc_2O_4:Eu^{2+}$. (Figure 3.3) However, it cannot be concluded with certainty that the Voronoi area around activators is directly correlated to bandgap energies or the crystal field strength around the activator. However, based on the incapacity of the Voronoi area to correctly predict thermal quenching rates for $SrSc_2O_4$ and $YK_3Si_2O_7$, it can safely be concluded that the Voronoi area is not necessarily related to the absolute bandgap energies or auto-ionization energies.

A small Voronoi area reflects a small LE volume which is prone to interact with ligands from other sub-shells and induce a smaller LE rigidity. However, a larger Voronoi area reflects a LE occupying most of the available 3-dimensional space and less prone to experience the effect from other ligands inducing a high rigidity LE. Subsequently, the Euclidean distance as defined in Chapter 2 can be regarded as a correlation to the thermal fluctuation of an activator's LE; while A and B are fitted parameters attempting to include an auto-ionization quenching process. Finally,

the Voronoi area is hence regarded as the ability of a set of LEs to preserve its integrity and resist thermal fluctuations.

3.5 Conclusion

In summary, the Voronoi area of activators inserted in host phosphors has shown a positive correlation with thermal stability. More fundamentally, Voronoi areas computed around the effective CN of each activator is a descriptor of the LE rigidity. In total, 27 thermal quenching values of Ce^{3+}/Eu^{2+}-activated phosphors have been predicted with R^2 of 0.92.

Table 3.1. Compounds, Space group, activators, intrinsic CN, and thermal quenching resistance (TQR%) measured by the emission intensity or IQE at 150℃ relative to 25℃.

Compound	Space Group	Activator	Exp 100-TQ%	Voronoi Area	Refs
$Lu_3Al_5O_{12}$	$Ia\bar{3}d$	Ce^{3+}	97	88	28–30
$Ba_9Lu_2Si_6O_{24}$	$R\bar{3}$	Ce^{3+}	97	87	31
$Y_3Al_5O_{12}$	$Ia\bar{3}d$	Ce^{3+}	94	78	33–35
$Ca_3Sc_2Si_3O_{12}$	$Ia\bar{3}d$	Ce^{3+}	92	95	36–38
$SrMgAl_{10}O_{17}$	$P6_3/mmc$	Eu^{2+}	88	76	48,49
$KSrPO_4$	$Pnma$	Eu^{2+}	88	84	43
$Ba_9Y_2Si_6O_{24}$	$R\bar{3}$	Ce^{3+}	85	86.58	32
Sr_2LiAlO_4	$P2_1/m$	Eu^{2+}	80	74	12
$BaSi_2N_2O_2$	$Cmcm$	Eu^{2+}	79	72	58
$BaZrSi_3O_9$	$P6c2$	Eu^{2+}	75	75.4	51,52
$BaSc_2Si_3O_{10}$	$P2_1/m$	Eu^{2+}	75	60	41
$NaScSi_2O_6$	$C2/c$	Ce^{3+}	70	60	59,60
$Ba_2MgSi_2O_7$	$C2/c$	Eu^{2+}	73	67	39
$SrLiPO_4$	$P6_3$	Eu^{2+}	68	64	61
$BaLu_2Si_3O_{10}$	$P2_1/m$	Ce^{3+}	62	70	40
$Sr_3P_2O_8$	$R\bar{3}m$	Eu^{2+}	60	47	62
$Ba_3P_2O_8$	$R\bar{3}m$	Eu^{2+}	55	44	62
$CaSc_2O_4$	$Pnma$	Ce^{3+}	50	47	63,64
Ca_2SiO_4	$Pmcm$	Eu^{2+}	44	40	42
Sr_2SiO_4	$P2_1/c$	Eu^{2+}	39	39	42
$BaLu_2Si_3O_{10}$	$P2_1/m$	Eu^{2+}	38	45	41
$Sr_2Al_2SiO_7$	$P\bar{4}2_1m$	Eu^{2+}	36	44	45–47
$NaCa_9MgP_7O_{28}$	$R3c$	Eu^{2+}	33	41	65,66
Ba_2SiO_4	$Pmcm$	Eu^{2+}	31	45	42
$Ca_6BaP_4O_{17}$	$C2/m$	Eu^{2+}	18	17	44
$Ca_3P_2O_8$	$R3c$	Eu^{2+}	10	10	67
$Sr_2MgSi_2O_7$	$P\bar{4}2_1m$	Eu^{2+}	10	5	68
$Ca_7Mg(SiO_4)_4$	$Pnn2$	Eu^{2+}	40	34.5	53
$CaMgSi_2O_6$	$Pmcm$	Eu^{2+}	15	26	53

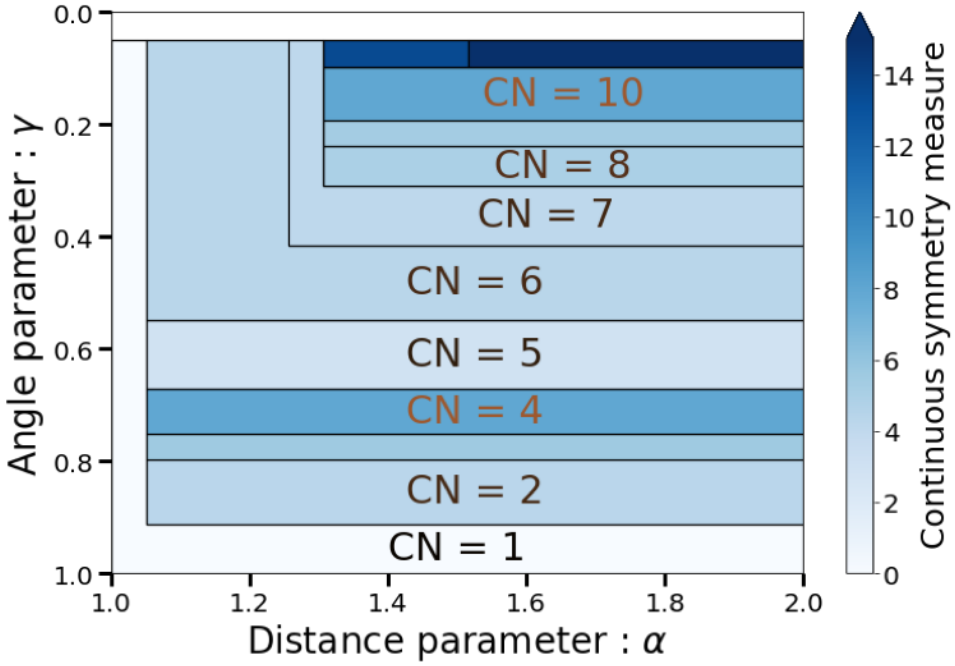

Figure 3.1 Voronoi Tessellation or Voronoi Grid Surface of Eu^{2+} doped in Sr_2SiO_4.
The Voronoi Grid Surface has two variables: the angle parameter, and the distance parameter. For a specific range of angle parameter and distance parameter a unique CN is defined. Each Voronoi grid is representative of a specific set of ligands denoted by a CN. Moreover, each grid's area is proportional to the three-dimensional volume available for the relevant set of ligands. Additionally, each Voronoi grid is decorated by a continuous symmetry measure (CSM) assessing the degree of each LE distortion. For clarification purposes, The Voronoi grid surface only computes the range of CN around the ECoN. The total area occupied by the set of CN: 4,5, and 6 is 39.25%. The reader can re@ferback to Table 2.1 for the ECoN of Eu^{2+} in Sr_2SiO_4.

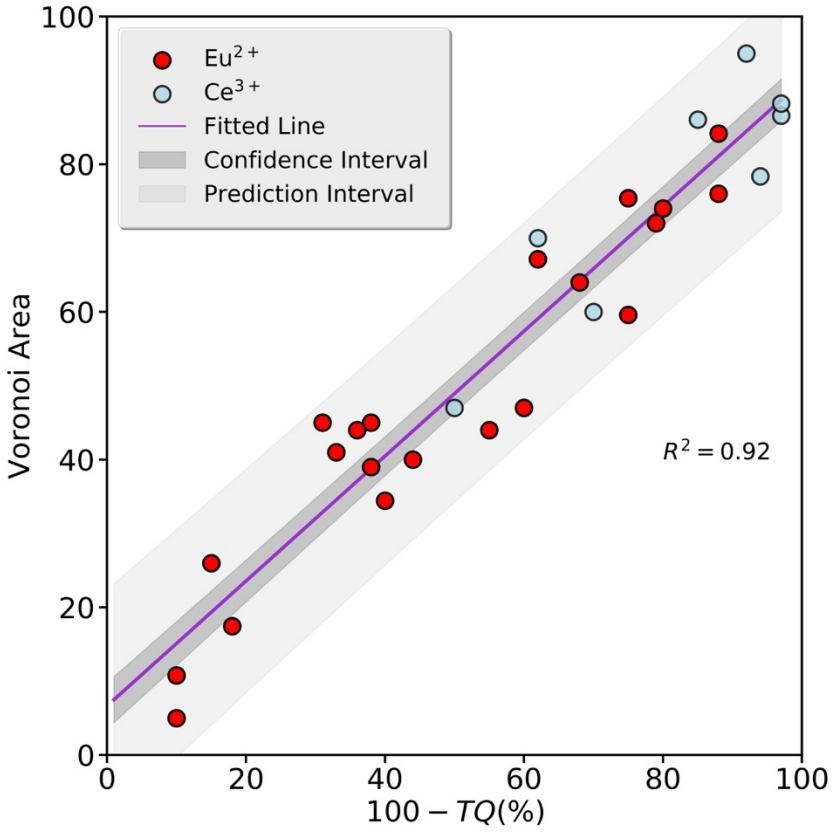

Figure 3.2 A plot of Voronoi area versus 100-TQ(%) for 27 oxide compounds.
Details on the 29 compounds considered in this analysis are included in the SI. The computed Voronoi area around the ECoN is able to predict thermal quenching resistance values with R-squared value of 0.92.

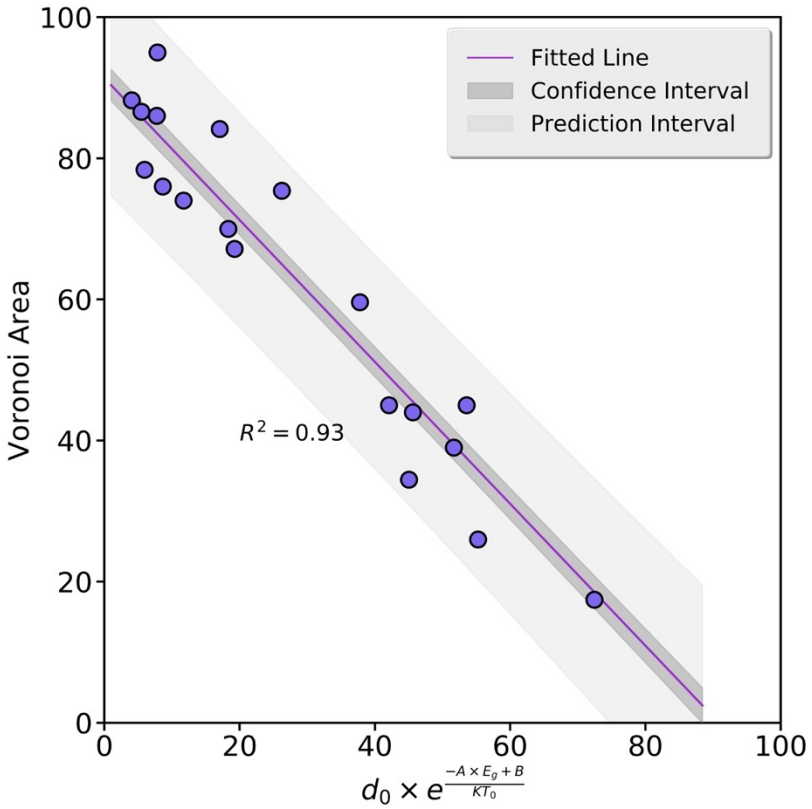

Figure 3.3 Voronoi Area as a function of Equation 2 fitting. The R-squared value is 0.94.
This plots only covers only 19 compounds on which AIMD simulations were computed on; omitting $SrSc_2O_4:Eu^{2+}$.

Chapter 4 Summary and Outlook

An innovative thermal quenching prediction scheme for oxide phosphors doped with Eu^{2+} and Ce^{3+} is outlined. Ab-initio molecular dynamics (AIMD) simulations and advanced LE assessments revealed that Eu^{2+}/Ce^{3+} LE rigidity and hosts electronic properties are climacteric to understanding and appraising thermal quenching. Computational thermal quenching predictions are found to mainly revolve on the ability to define the most relevant LE around an activator. Hoppe's effective CN, geometrical bond strength as described by bond weights, electron density distribution around the activator and ligands as defined by bond orders and the continuous symmetry measure (CSM) – all contribute to defining and probing LEs fluctuations at 300 and 500 K. A linear fitting between the Euclidean distance (Equation 1) and experimental thermal quenching for 20 well-known compounds is found to have an R^2 value of 0.57. The low accuracy from the Euclidean distance predictions is explained by the presence of a diverse range of PBE bandgap energies within the 20 doped hosts. Inspired from the auto-ionization model proposed from Dorenbos; the Euclidean distance and auto-ionization process are treated as two independent events resulting in a singular rate, namely the thermal quenching rate. It assumed that auto-ionization rates are partially linked to PBE bandgap energies, and Euclidean distances are relative measurements of LEs rigidity. Therefore, using PBE bandgap energies as an auto-ionization *proxy,* and Euclidean distances as a LE rigidity descriptor; an Arrhenius-type equation is developed where the pre-exponential factor is the computed Euclidean distance, and the commonly known 'activation energy' was linearly fitted using PBE bandgap energies. The R^2 value obtained from the Arrhenius equation is of 0.95. Moreover, an intrinsic Voronoi area around the effective CN is used to correctly predict the thermal quenching of 29 compounds with an R^2 value of 0.92. Finally, based on the results found in this study, it becomes evident that developing a new red

oxide phosphor with high thermal stability requires discovering a red phosphor with a high LER. The development of Voronoi area predictions promises a fast screening tool, and the development of a thermally stable red-emission oxide, which will undeniably reduce WLED costs.

The full content of this thesis is currently being prepared for submission for publication of the material. Wang, tang, Chen, and Ong. The thesis author was the primry investigator and author of this material.

References

(1) Inc. Navigant Consulting *Energy savings forecast of solid-state lighting in general illumination applications*, U.S. Dep. Energy Rep., 2014, 2013–2014.

(2) Bardsley, Norman ; Hansen, Monica; Pattison, Lisa ; Pattison, Morgan ;Stober, Kelsey ;Taylor, Victor; Tsao,Jeffrey ;Yamada, M. *Solid-State Lighting R&D Plan*; 2016.

(3) Yen, W.; Weber, M. *Inorganic Phosphors*; CRC Press, 2004.

(4) 2018 Solid-State Lighting R & D Opportunities, 2019.

(5) Li, G.; Tian, Y.; Zhao, Y.; Lin, J. *Recent progress in luminescence tuning of Ce^{3+} and Eu^{2+} -activated phosphors for pc-WLEDs*, Chem. Soc. Rev., 2015, *44*, 8688–8713, doi:10.1039/C4CS00446A.

(6) Ronda, C. R. Emission and Excitation Mechanisms of Phosphors; 2007.

(7) Edition, S. *III-Nitride Based Light Emitting Diodes and Applications*; Seong, T.-Y.; Han, J.; Amano, H.; Morkoç, H., Eds.; Topics in Applied Physics; Springer Singapore: Singapore, 2017; Vol. 133.

(8) Wang, L.; Jin, J.; Mi, C.; Hao, Z.; Luo, Y.; Sun, C.; Han, Y.; Xiong, B.; Wang, J.; Li, H. *A review on experimental measurements for understanding efficiency droop in InGaN-based light-emitting diodes*, Materials (Basel)., 2017, *10*, doi:10.3390/ma10111233.

(9) Lin, C. C.; Chen, W.; Liu, R. S. *Handbook of Advanced Lighting Technology*; 2017.

(10) Chaudhry, A.; Boutchko, R.; Chourou, S.; Zhang, G.; Grønbech-Jensen, N.; Canning, A. *First-principles study of luminescence in Eu^{2+}-doped inorganic scintillators*, Phys. Rev. B - Condens. Matter Mater. Phys., 2014, *89*, 155105, doi:10.1103/PhysRevB.89.155105.

(11) Burns, R. G.; Burns, R. G. *Outline of crystal field theory*; 2009.

(12) Wang, Z.; Ha, J.; Kim, Y. H.; Im, W. Bin; McKittrick, J.; Ong, S. P. *Mining Unexplored Chemistries for Phosphors for High-Color-Quality White-Light-Emitting Diodes*, Joule, 2018, *2*, 914–926, doi:10.1016/j.joule.2018.01.015.

(13) Li, G.; Tian, Y.; Zhao, Y.; Lin, J. *Recent progress in luminescence tuning of Ce^{3+} and Eu<sub>2+</sup> -activated phosphors for pc-WLEDs*, Chem. Soc. Rev., 2015, *44*, 8688–8713, doi:10.1039/C4CS00446A.

(14) Blasse, G.; Bril, A. *Characteristic luminescence*, Phil. Tech. Rev., 1970, *31*, 304–314.

(15) Blasse, G.; Grabmaier, B. C. *Luminescent Materials*; Springer Berlin Heidelberg: Berlin, Heidelberg, 1994.

(16) Dorenbos, P. *Thermal quenching of Eu^{2+} 5*d*–4*f *luminescence in inorganic compounds*, J. Phys. Condens. Matter, 2005, *17*, 8103–8111, doi:10.1088/0953-8984/17/50/027.

(17) Denault, K. A.; Brgoch, J.; Kloß, S. D.; Gaultois, M. W.; Siewenie, J.; Page, K.; Seshadri, R. *Average and local structure, debye temperature, and structural rigidity in some oxide compounds related to phosphor hosts*, ACS Appl. Mater. Interfaces, 2015, *7*, 7264–7272, doi:10.1021/acsami.5b00445.

(18) Ha, J.; Wang, Z.; Novitskaya, E.; Hirata, G. A.; Graeve, O. A.; Ong, S. P.; McKittrick, J. An integrated first principles and experimental investigation of the relationship between structural rigidity and quantum efficiency in phosphors for solid state lighting, J. Lumin., 2016, 179, 297–305, doi:10.1016/j.jlumin.2016.07.006.

(19) Ong, S. P.; Richards, W. D.; Jain, A.; Hautier, G.; Kocher, M.; Cholia, S.; Gunter, D.; Chevrier, V. L.; Persson, K. A.; Ceder, G. *Python Materials Genomics (pymatgen): A robust, open-source python library for materials analysis*, Comput. Mater. Sci., 2013, *68*, 314–319, doi:10.1016/j.commatsci.2012.10.028.

(20) Wang, Z. Design and Optimization of Phosphors for Solid-State Lighting using First-Principles Calculations A dissertation submitted in partial satisfaction of the requirements for the degree Doctor of Philosophy in NanoEngineer, University of California, San Diego, 2018.

(21) Kresse, G.; Furthmüller, J. *Efficient iterative schemes for ab initio total-energy calculations using a plane-wave basis set*, Phys. Rev. B, 1996, *54*, 11169–11186, doi:10.1103/PhysRevB.54.11169.

(22) Blöchl, P. E. *Projector augmented-wave method*, Phys. Rev. B, 1994, *50*, 17953–17979, doi:10.1103/PhysRevB.50.17953.

(23) Perdew, J. P.; Burke, K.; Ernzerhof, M. *Generalized Gradient Approximation Made Simple*, Phys. Rev. Lett., 1996, *77*, 3865–3868, doi:10.1103/PhysRevLett.77.3865.

(24) Jain, A.; Ong, S. P.; Hautier, G.; Chen, W.; Richards, W. D.; Dacek, S.; Cholia, S.; Gunter, D.; Skinner, D.; Ceder, G.; Persson, K. A. *Commentary: The materials project: A materials*

genome approach to accelerating materials innovation, APL Mater., 2013, *1*, 011002, doi:10.1063/1.4812323.

(25) Dudarev, S. L.; Botton, G. A.; Savrasov, S. Y.; Humphreys, C. J.; Sutton, A. P. *Electron-energy-loss spectra and the structural stability of nickel oxide: An LSDA+U study*, Phys. Rev. B, 1998, *57*, 1505–1509, doi:10.1103/PhysRevB.57.1505.

(26) Hoover, W. G. Hoover WG (1985) Canonical dynamics: Equilibrium phase-space distributions. Phys Rev A 31:1695–1697 . doi: 10.1103/PhysRevA.31.1695, 1985, 31, 1695–1697.

(27) Hoppe, R. *The CN*, 1970, *9*, 25–34.

(28) Park, K.; Kim, T.; Yu, Y.; Seo, K.; Kim, J. *Y/Gd-free yellow $Lu_3Al_5O_{12}:Ce^{3+}$ phosphor for white LEDs*, J. Lumin., 2016, *173*, 159–164, doi:10.1016/j.jlumin.2016.01.014.

(29) Xu, J.; Chen, W.; Zeng, R.; Peng, D. A carbon-free sol-gel method for preparation of $Lu_3Al_5O_{12}$: Ce^{3+} phosphors for potential applications in laser scintillators and LEDs, Mater. Lett., 2014, 133, 1–4, doi:10.1016/j.matlet.2014.06.030.

(30) Song, Y.-H.; Chung, E.-J.; Jung, M.-K.; Masaki, T.; Senthil, K.; Lee, S.-J.; Yoo, J.-S.; Yoon, D.-H. Enhancement of optical characteristics of green-emitting single-phase $Lu_3Al_5O_{12}$: Ce^{3+} phosphor using $CeO_2@B_2O_3$ core–shell for white light generation, Mater. Lett., 2014, 116, 337–340, doi:10.1016/j.matlet.2013.11.022.

(31) Liu, Y.; Silver, J.; Xie, R.-J.; Zhang, J.; Xu, H.; Shao, H.; Jiang, J.; Jiang, H. *An excellent cyan-emitting orthosilicate phosphor for NUV-pumped white LED application*, J. Mater. Chem. C, 2017, *5*, 12365–12377, doi:10.1039/C7TC04168C.

(32) Brgoch, J.; Borg, C. K. H.; Denault, K. A.; Mikhailovsky, A.; Denbaars, S. P.; Seshadri, R. *An efficient, thermally stable cerium-based silicate phosphor for solid state white lighting*, Inorg. Chem., 2013, *52*, 8010–8016, doi:10.1021/ic400614r.

(33) Jang, H. S.; Won, Y. H.; Jeon, D. Y. *Improvement of electroluminescent property of blue LED coated with highly luminescent yellow-emitting phosphors*, Appl. Phys. B Lasers Opt., 2009, *95*, 715–720, doi:10.1007/s00340-009-3484-1.

(34) Chen, L.; Lin, C. C.; Yeh, C. W.; Liu, R. S. *Light converting inorganic phosphors for white light-emitting diodes*, Materials (Basel)., 2010, *3*, 2172–2195, doi:10.3390/ma3032172.

(35) Ueda, J.; Dorenbos, P.; Bos, A. J. J.; Meijerink, A.; Tanabe, S. *Insight into the Thermal Quenching Mechanism for $Y_3Al_5O_{12}:Ce^{3+}$ through Thermoluminescence Excitation Spectroscopy*, J. Phys. Chem. C, 2015, *119*, 25003–25008, doi:10.1021/acs.jpcc.5b08828.

(36) Akai, T.; Shigeiwa, M.; Okamoto, K.; Shimomura, Y.; Kijima, N.; Honma, T. *XAFS analysis of local structure around Ce in $Ca_3Sc_2Si_3O_{12}$:Ce phosphor for white LEDs*, AIP Conf. Proc., 2007, *882*, 389–391, doi:10.1063/1.2644534.

(37) Shimomura, Y.; Honma, T.; Shigeiwa, M.; Akai, T.; Okamoto, K.; Kijima, N. *Photoluminescence and Crystal Structure of Green-Emitting $Ca_3Sc_2Si_3O_{12}:Ce^{3+}$ Phosphor for White Light Emitting Diodes*, J. Electrochem. Soc., 2007, *154*, J35, doi:10.1149/1.2388856.

(38) I. Levchuk, F. Schröppel, L. Römling, A. Osvet, N. Khaidukov, Y. Zorenko, R. Van Deun, M. Batentschuk, C. J. B. Highly luminescent Ca3Sc2Si3O12:Ce3+ silicate garnet nano- and microparticles with 50-70% photoluminescence quantum yields as efficient phosphor converters for white LEDs https://www.techconnectworld.com/World2017/sym/Photonic_Materials_Devices.html.

(39) Zhang, X.; Zhang, J.; Wang, R.; Gong, M. *Photo-Physical Behaviors of Efficient Green Phosphor $Ba_2MgSi_2O_7:Eu^{2+}$ and Its Application in Light-Emitting Diodes*, J. Am. Ceram. Soc., 2010, *93*, 1368–1371, doi:10.1111/j.1551-2916.2009.03549.x.

(40) Li, K.; Liang, S.; Lian, H.; Shang, M.; Xing, B.; Lin, J. *Ce^{3+} and Tb^{3+}-doped lutetium-containing silicate phosphors: Synthesis, structure refinement and photoluminescence properties*, J. Mater. Chem. C, 2016, *4*, 3443–3453, doi:10.1039/c6tc00579a.

(41) Brgoch, J.; Hasz, K.; Denault, K. A.; Borg, C. K. H.; Mikhailovsky, A. A.; Seshadri, R. Data-driven discovery of energy materials: Efficient $BaM_2Si_3O_{10}$: Eu^{2+} (M = Sc, Lu) phosphors for application in solid state white lighting, Faraday Discuss., 2014, 176, 333–347, doi:10.1039/c4fd00125g.

(42) Kim, J. S.; Park, Y. H.; Kim, S. M.; Choi, J. C.; Park, H. L. *Temperature-dependent emission spectra of $M_2SiO_4:Eu^{2+}$(M=Ca, Sr, Ba) phosphors for green and greenish white LEDs*, Solid State Commun., 2005, *133*, 445–448, doi:10.1016/j.ssc.2004.12.002.

(43) Tang, Y. S.; Hu, S. F.; Lin, C. C.; Bagkar, N. C.; Liu, R. S. *Thermally stable luminescence of $KSrPO_4:Eu^{2+}$ phosphor for white light UV light-emitting diodes*, Appl. Phys. Lett., 2007, *90*, 4–6, doi:10.1063/1.2721846.

(44) Komuro, N.; Mikami, M.; Shimomura, Y.; Bithell, E. G.; Cheetham, A. K. Synthesis, structure and optical properties of cerium-doped calcium barium phosphate-a novel blue-green phosphor for solid-state lighting, J. Mater. Chem. C, 2015, 3, 204–210, doi:10.1039/c4tc01835d.

(45) Li, Y. Q.; Hirosaki, N.; Xie, R. J.; Mitomo, M. *Crystal, electronic and luminescence properties of Eu2+-doped Sr2Al2-xSi1+xO7-xNx*, Sci. Technol. Adv. Mater., 2007, *8*, 607–616, doi:10.1016/j.stam.2007.08.007.

(46) Lu, F.-C.; Bai, L.-J.; Dang, W.; Yang, Z.-P.; Lin, P. *Structure and Photoluminescence of Eu^{2+} Doped $Sr_2Al_2SiO_7$ Cyan-Green Emitting Phosphors*, ECS J. Solid State Sci. Technol., 2014, *4*, R27–R30, doi:10.1149/2.0151502jss.

(47) Zhou, W.; Ma, X.; Zhang, M.; Luo, Y.; Xia, Z. *Effect of different RE dopants on phosphorescence properties of $Sr_2Al_2SiO_7:Eu^{2+}$ phosphors*, J. Rare Earths, 2015, *33*, 700–705, doi:10.1016/S1002-0721(14)60473-7.

(48) Onuma, H.; Student, S. I. D.; Carpio, C. A. Del *Host emission from $BaMgAl_{10}O_{17}$ and $SrMgAl_{10}O_{17}$ phosphor :*, 2010, 211–222.

(49) Wang, L.; Zhang, H.; Li, Y.; Liang, P.; Shen, Y.; Jiao, F. *Enhanced luminescence in the $SrMgAl_{10}O_{17}$: Eu^{2+} blue phosphor prepared by a hybrid urea-sol combustion route*, Int. J. Appl. Ceram. Technol., 2016, *13*, 185–190, doi:10.1111/ijac.12420.

(50) Müller, M.; Volhard, M. F.; Jüstel, T. *Photoluminescence and afterglow of deep red emitting $SrSc_2O_4$:Eu^{2+}*, RSC Adv., 2016, *6*, 8483–8488, doi:10.1039/c5ra25686k.

(51) Wang, D. Y.; Huang, C. H.; Wu, Y. C.; Chen, T. M. *$BaZrSi_3O_9$:Eu^{2+}: A cyan-emitting phosphor with high quantum efficiency for white light-emitting diodes*, J. Mater. Chem., 2011, *21*, 10818–10822, doi:10.1039/c1jm00080b.

(52) Komukai, T.; Takatsuka, Y.; Kato, H.; Kakihana, M. *Luminescence properties of $BaZrSi_3O_9$:Eu synthesized by an aqueous solution method*, J. Lumin., 2015, *158*, 328–332, doi:10.1016/j.jlumin.2014.10.021.

(53) Ha, J.; Wang, Z.; Novitskaya, E.; Hirata, G. A.; Graeve, O. A.; Ong, S. P.; McKittrick, J. An integrated first principles and experimental investigation of the relationship between structural rigidity and quantum efficiency in phosphors for solid state lighting, J. Lumin., 2016, 179, 297–305, doi:10.1016/j.jlumin.2016.07.006.

(54) O'Keeffe, M. *A proposed rigorous definition of CN*, Acta Crystallogr. Sect. A, 1979, *35*, 772–775, doi:10.1107/S0567739479001765.

(55) Waroquiers, D.; Gonze, X.; Rignanese, G. M.; Welker-Nieuwoudt, C.; Rosowski, F.; Göbel, M.; Schenk, S.; Degelmann, P.; André, R.; Glaum, R.; Hautier, G. *Statistical analysis of coordination environments in Oxides*, Chem. Mater., 2017, *29*, 8346–8360, doi:10.1021/acs.chemmater.7b02766.

(56) Pinsky, M.; Avnir, D. *Continuous Symmetry Measures. 5. The Classical Polyhedra*, Inorg. Chem., 2002, *37*, 5575–5582, doi:10.1021/ic9804925.

(57) Zhuo, Y.; Mansouri Tehrani, A.; Oliynyk, A. O.; Duke, A. C.; Brgoch, J. *Identifying an efficient, thermally robust inorganic phosphor host via machine learning*, Nat. Commun., 2018, *9*, doi:10.1038/s41467-018-06625-z.

(58) Bachmann, V.; Ronda, C.; Oeckler, O.; Schnick, W.; Meijerink, A. *Color point tuning for (Sr,Ca,Ba)Si2O2N 2:Eu2+ for white light LEDs*, Chem. Mater., 2009, *21*, 316–325, doi:10.1021/cm802394w.

(59) Min, J.; Yamaguchi, T.; Kato, H.; Kobayashi, M.; Yamane, H.; Kakihana, M. *Development of two novel Eu2+-activated phosphors in the Na-Sc-Si-O system and their photoluminescence properties*, J. Lumin., 2014, *154*, 285–289, doi:10.1016/j.jlumin.2014.05.006.

(60) Xia, Z.; Zhang, Y.; Molokeev, M. S.; Atuchin, V. V. Structural and luminescence properties of yellow-emitting $NaScSi_2O_6:Eu^{2+}$ phosphors:Eu^{2+} Site preference analysis and generation of red emission by codoping Mn^{2+} for white-light-emitting diode applicat, J. Phys. Chem. C, 2013, 117, 20847–20854, doi:10.1021/jp4062225.

(61) Lin, C. C.; Xiao, Z. R.; Guo, G.-Y.; Chan, T.-S.; Liu, R.-S. Versatile Phosphate Phosphors $ABPO_4$ in White Light-Emitting Diodes: Collocated Characteristic Analysis and Theoretical Calculations, J. Am. Chem. Soc., 2010, 132, 3020–3028, doi:10.1021/ja9092456.

(62) Ji, H.; Huang, Z.; Xia, Z.; Molokeev, M. S.; Atuchin, V. V.; Fang, M.; Liu, Y. Discovery of new solid solution phosphors via cation substitution-dependent phase transition in $M_3(PO_4)_2:Eu^{2+}$ (M = Ca/Sr/Ba) quasi-binary sets, J. Phys. Chem. C, 2015, 119, 2038–2045, doi:10.1021/jp509743r.

(63) George, N. C.; Brgoch, J.; Pell, A. J.; Cozzan, C.; Jaffe, A.; Dantelle, G.; Llobet, A.; Pintacuda, G.; Seshadri, R.; Chmelka, B. F. *Correlating Local Compositions and Structures with the Macroscopic Optical Properties of Ce^{3+}-Doped $CaSc_2O_4$, an Efficient Green-Emitting Phosphor*, Chem. Mater., 2017, *29*, 3538–3546, doi:10.1021/acs.chemmater.6b05394.

(64) Sharma, S. K.; Bettinelli, M.; Carrasco, I.; Karlsson, M. Influence of Ce^{3+} Concentration on the Thermal Stability and Charge-Trapping Dynamics in the Green Emitting Phosphor $CaSc_2O_4:Ce^{3+}$, J. Phys. Chem. C, 2017, 121, 23096–23103, doi:10.1021/acs.jpcc.7b08263.

(65) Xia, Z.; Liu, H.; Li, X.; Liu, C. Identification of the crystallographic sites of Eu^{2+} in $Ca_9NaMg(PO_4)_7$: Structure and luminescence properties study, Dalt. Trans., 2013, 42, 16588–16595, doi:10.1039/c3dt52232f.

(66) Hou, J.; Yin, X.; Fang, Y.; Huang, F.; Jiang, W. *Emission-tunable phosphors $Ca_9MgM'(PO_4)_7:Eu^{2+},Mn^{2+}$ (M'=Li, Na, K) for white light-emitting diodes*, J. Lumin., 2012, *132*, 1307–1310, doi:10.1016/j.jlumin.2011.12.071.

(67) Ji, H.; Huang, Z.; Xia, Z.; Molokeev, M. S.; Chen, M.; Atuchin, V. V.; Fang, M.; Liu, Y.; Wu, X. Phase Transformation in $Ca_3(PO_4)_2:Eu^{2+}$ via the Controlled Quenching and Increased Eu^{2+} Content: Identification of New Cyan-Emitting alpha-$Ca_3(PO_4)_2:Eu^{2+}$, J. Am. Ceram. Soc., 2015, 98, 3280–3284, doi:10.1111/jace.13787.

(68) Hölsä, J.; Kirm, M.; Laamanen, T.; Lastusaari, M.; Niittykoski, J.; Novák, P. *Electronic structure of the $Sr_2MgSi_2O_7:Eu^{2+}$ persistent luminescence material*, J. Lumin., 2009, *129*, 1560–1563, doi:10.1016/j.jlumin.2009.04.042.